RSC Advances

PAPER

View Article Online
View Journal | View Issue

Cite this: *RSC Adv.*, 2026, **16**, 22422

Enhanced removal of fluoride and phosphate by nickel-doped kaolinite nano-adsorbents: mechanisms and resource recovery

Asmaa S. Morshedy, *[a] Tahany Mahmoud, *[b] Aya M. Matloob[a] and Mahmoud F. Mubarak[b]

The development of efficient and cost-effective catalysts for wastewater treatment is crucial for mitigating environmental pollution. In this study, NiO and Ni-metal doped kaolinite-based nanocomposites were synthesized *via* precipitation and calcination methods and evaluated for fluoride (F^-) and phosphate (PO_4^{3-}) remediation. Comprehensive characterization was performed using X-ray diffraction (XRD), Fourier transform infrared spectroscopy (FT-IR), scanning electron microscopy-energy dispersive X-ray spectroscopy (SEM-EDX), Raman spectroscopy, Brunauer–Emmett–Teller (BET), and dynamic light scattering (DLS) analyses. The adsorption performance was systematically examined under varying pH, initial pollutant concentration, contact time, temperature, and adsorbent dosage. The $Ni(OH)_2$@kaolinite composite exhibited the highest adsorption capacities: 52.6 mg g^{-1} for fluoride and 55.0 mg g^{-1} for phosphate, with over 90% removal efficiency under optimal conditions. Kinetic data were best described by the pseudo second order model, indicating that the adsorption rate depends on the availability of active sites and adsorption capacity; however, kinetic fitting alone was not used to assign the adsorption mechanism, which was further evaluated using diffusion and thermodynamic analyses. The composites demonstrated excellent reusability, retaining over 75% efficiency after 10 cycles. Compared to conventional adsorbents, the Ni-doped kaolinite showed superior performance and cost-effectiveness (estimated treatment cost: <$5 per 1000 L), highlighting its potential as a sustainable, scalable solution for industrial wastewater treatment and resource recovery.

Received 14th January 2026
Accepted 17th April 2026

DOI: 10.1039/d6ra00357e

rsc.li/rsc-advances

1. Introduction

Water contamination due to industrial discharge remains a major environmental challenge, particularly the presence of toxic organic and inorganic pollutants. Among various remediation strategies, heterogeneous catalysis has emerged as an effective and sustainable approach for wastewater treatment. The design of cost-effective, stable, and highly active catalysts is essential for improving pollutant degradation efficiency while ensuring reusability and environmental sustainability.[1–4]

The removal of fluoride (F^-) and phosphate (PO_4^{3-}) from wastewater is critical due to their harmful environmental and health impacts. Excessive fluoride causes dental/skeletal fluorosis, while phosphate contributes to eutrophication, disrupting aquatic ecosystems. Traditional methods like precipitation and ion exchange are often inefficient or costly, prompting the development of advanced adsorbents for selective and sustainable remediation.[5]

Clay-based composites, such as metal–oxide-functionalized clays exhibit high affinity for F^-, and PO_4^{3-} through ligand exchange and electrostatic-interactions. For instance, La-modified bentonite achieves >95% fluoride removal *via* formation of La–F complexes, while Fe-coated clays adsorb phosphate through inner-sphere complexation.[5–7] Chitosan–alginate hydrogels and biochar composites further enhance adsorption capacity (50–120 mg g^{-1} for F^- and 40–100 mg g^{-1} for PO_4^{3-}) while offering reusability (more than 5 cycles). Innovations like ZrO_2 nanoparticles or layered double hydroxides (LDHs) improve selectivity in mixed-anion systems.

Coupling these materials with membrane filtration or electrocoagulation boosts efficiency, reducing residual concentrations below World Health Organization (WHO) limits (<1.5 mg L^{-1} F^-, <0.1 mg L^{-1} PO_4^{3-}). Future research should optimize scalability, cost, and regeneration protocols to bridge lab-scale success with industrial adoption, ensuring compliance with stringent water-quality standards.

Nickel-based catalysts (Ni and NiO) are particularly attractive for wastewater treatment due to their strong redox properties, excellent catalytic activity, and affordability compared to noble metal catalysts.[6–8] However, the interaction between the active metal species and the clay support plays a critical role in

[a]*Refining Department, Egyptian Petroleum Research Institute, 11727, Cairo, Egypt. E-mail: asma_2000asma@yahoo.com*

[b]*Petroleum Application Department, Egyptian Petroleum Research Institute, 11727, Cairo, Egypt. E-mail: tahany.mahmoud.a@gmail.com*

determining catalytic efficiency, necessitating a deeper investigation into their behavior.[9–13]

In this study, NiO@kaolinite and Ni@kaolinite catalysts were synthesized and systematically evaluated for their catalytic performance in wastewater treatment. The materials were characterized using XRD, FT-IR, SEM-EDX, and BET to understand their structural, morphological, and compositional properties. To gain insight into their catalytic behavior, a comparative kinetic study was conducted to determine the reaction order and degradation mechanisms. Furthermore, statistical modeling was applied to assess the influence of key operational parameters such as pollutant concentration, temperature, pH, and catalyst dosage on wastewater treatment efficiency. The reusability and stability of the catalysts over multiple cycles were also investigated to evaluate their practical applicability.

This study aims to provide a comprehensive understanding of NiO and Ni-modified clay-based catalysts for wastewater treatment by integrating kinetic analysis, statistical modeling, and thermodynamic evaluation. The findings will contribute to the development of efficient, cost-effective, and environmentally friendly catalysts for industrial wastewater remediation.

2. Experimental

2.1. Materials

Nickel nitrate hexahydrate ($Ni(NO_3)_2 \cdot 6H_2O$, ≥98% purity), ammonium hydroxide (NH_3, 33%), and kaolinite (clay ≥98% purity) were purchased from Sigma-Aldrich (United Kingdom). All chemicals were used without further treatment.

2.2. Chemical treatment for kaolinite support

The acid treatment was performed using 6 mol per liter sulfuric acid solution for 3 hours at 90 °C under reflux with continuous stirring.[14,15] A solid-to-liquid ratio of 5 g of kaolinite per 150 mL of acid solution was maintained.[16] Following the treatment, the sample was washed with distilled water until it reached a neutral pH, then dried at 100 °C for 48 hours. The dried material was then subjected to peroxide treatment.[17] The sample was treated with 35% (v/v) hydrogen peroxide at 25 °C for 3 hours, using solid to liquid ratio of 5 g of kaolinite per 100 mL of peroxide solution. Afterward, it was thoroughly washed with distilled water until neutral pH was achieved, then dried at 60 °C for 24 hours. Thermal treatment was conducted in a muffle furnace for 5 hours, where the sample was gradually heated from ambient temperature (25 °C) to 800 °C at a heating rate of 10 °C min^{-1}. After calcination, the sample was transferred to an oven at 100 °C, and then stored in a desiccator until it cooled to room temperature. Finally, the material was macerated and sieved using a 0.425 mm sieve (Tyler series), yielding sample K_T.

2.3. Synthesis of NiO@kaolinite and Ni@kaolinite nanocomposites

The corresponding composites were prepared following the simple precipitation method. Initially, 2 mmol of nickel nitrate hexahydrate ($Ni(NO_3)_2 \cdot 6H_2O$) was introduced into 1500 mL of distilled water containing 5 gram of treated kaolinite-support. The mixture stirred for 30 min, until a homogeneous solution was obtained. This mixed solution was titrated with ammonia solution until (pH = 10) and maintained at 80 °C for 1 h. The resulting faint green product was separated by filtration and washed several times by distilled water to remove any residual components. The product was dried at 60 °C to give $Ni(OH)_2$@kaolinite.[18] Finally, the powder was calcined by two different ways first at 500 °C for six hour in a muffle furnace and the second under the same conditions but under vacuum to give NiO@kaolinite and Ni@kaolinite, respectively.

2.4. Characterization tools

Several apparatuses of analysis were used to determine the vital characteristics of the prepared materials such as structural, morphological, and thermal features. X-ray diffraction (XRD) patterns were determined *via* Cu Kα X-ray radiation (Germany, λ = 1.540 Å, PANalytical X'PERT PRO). Fourier transform infrared spectroscopy (FT-IR) was used to detect the functional groups of samples from 4000 to 400 cm^{-1} using a PerkinElmer spectrometer *via* the KBr pellet method (Spectrum One, USA). The surface area of the as-synthesized materials is recorded by the adsorption–desorption isotherms of nitrogen at −196 °C (ANOVA 3200, USA). A high-resolution scanning electron microscope (HRSEM) was formfitting (JEOL, JSM [model no: 6360]) to confirm the morphological structure of the prepared samples. Dynamic Light Scattering (DLS) at 25 °C and a laser angle of 90° was used to determine the particle size distribution (Zetasizer Nano-ZS90 apparatus, Malvern Co., UK).

2.5. Parameters of application

2.5.1. Preparation of adsorbent and experimental setup. The adsorption experiments will be conducted in a batch mode to evaluate the efficiency of nickel-based nanoparticles (Ni, NiO, and $Ni(OH)_2$) doped kaolinite for removing fluoride (F^-) and phosphate (PO_4^{3-}) from aqueous solutions. The nanoparticles will be synthesized using a chemical precipitation method, followed by characterization through XRD, SEM mapping-EDX, BET surface area analysis, and FT-IR to determine their structural, morphological, and surface properties.

2.5.2. Effect of initial concentration. Fluoride and phosphate solutions with varying initial concentrations (5–100 mg L^{-1}) will be prepared to study the effect of contaminant concentration. The adsorption capacity and removal efficiency will be analyzed at each concentration to determine the equilibrium adsorption isotherm. This parameter helps understand the nanomaterial's adsorption capacity at different pollutant loadings.

2.5.3. Effect of contact time and kinetics study. Adsorption kinetics will be evaluated by varying the contact time (5–180 min) while keeping all other parameters constant. Samples will be collected at different intervals and analyzed to determine the adsorption rate. The kinetic data will be fitted to pseudo first order, pseudo second order, and intra-particle diffusion models to identify the dominant adsorption mechanism.[19]

2.5.4. Effect of solution pH. Since pH significantly influences the surface charge of adsorbents and ionization of fluoride and phosphate species, the adsorption behavior will be studied over a pH range of 2–12. Adjustments will be made using 0.1 M HCl or NaOH, and the adsorbents' point of zero charge (pH_{pzc}) will be determined to explain the adsorption mechanism.

2.5.5. Effect of adsorbent dosage. The optimal amount of adsorbent required for maximum contaminant removal will be determined by varying the adsorbent dose (0.1–5.0 g L^{-1}). The results will reveal the relationship between nanoparticle adsorption capacity and available active sites.[20]

2.5.6. Effect of temperature and thermodynamics study. To examine the influence of temperature, adsorption experiments will be conducted at different temperatures (298, 308, 318, and 328 K). Thermodynamic parameters such as Gibbs free energy ($\Delta G°$), enthalpy ($\Delta H°$), and entropy ($\Delta S°$) will be calculated to determine whether the adsorption process is spontaneous and endothermic or exothermic.

2.5.7. Adsorption isotherm analysis. The equilibrium adsorption data will be analyzed using Langmuir, Freundlich, and Temkin isotherm models to determine the adsorption mechanism and capacity. The Langmuir isotherm will indicate monolayer adsorption, whereas the Freundlich isotherm will suggest multilayer adsorption on heterogeneous surfaces.[21–24]

2.5.8. Effect of co-existing ions and selectivity study. Since natural water contains competing ions, the selectivity of the nickel-based nanoparticles toward fluoride and phosphate in the presence of chloride (Cl^-), sulfate (SO_4^{2-}), nitrate (NO_3^-), and carbonate (CO_3^{2-}) will be examined. The interference effect of these ions will be analyzed to assess the practical applicability of the adsorbents in real water treatment scenarios.

2.5.9. Regeneration and reusability study. Regeneration and reusability are crucial for determining an adsorbent's economic feasibility and sustainability for water treatment applications. A highly efficient adsorbent should exhibit high initial adsorption capacity and retain its performance over multiple adsorption–desorption cycles. In this study, the regeneration ability of nickel-based nanoparticles (Ni, NiO, and $Ni(OH)_2$) for fluoride (F^-) and phosphate (PO_4^{3-}) removal will be systematically evaluated. The primary goal is to assess these contaminants' desorption efficiency and the adsorbent's stability after multiple reuses.

To regenerate the spent adsorbents, various desorption agents will be tested to determine their effectiveness in removing fluoride and phosphate. Alkaline solutions such as NaOH, KOH, and $Ca(OH)_2$ (pH 10–12) will disrupt the electrostatic interactions between the adsorbed ions and the adsorbent surface. Acidic solutions (HCl, H_2SO_4, pH 2–4) will also be investigated, as they can protonate functional groups and weaken the attraction between the adsorbate and adsorbent. Additionally, salt solutions such as NaCl, $NaNO_3$, and Na_2SO_4 (0.1–1.0 M) will induce competitive ion exchange and promote desorption. Simple distilled water washes will be tested as a control to evaluate the weakly bound fluoride and phosphate fraction. The effect of pH on desorption will be studied to identify optimal conditions for regenerating the adsorbents. By varying the pH from 2 to 12, the influence of protonation and deprotonation on the release of contaminants will be examined. A highly efficient regeneration process should achieve maximum desorption at minimal chemical consumption, ensuring economic viability. Desorption efficiency will be calculated based on the concentration of fluoride and phosphate released into the desorbing solution, which will be measured using ion chromatography (IC) or spectrophotometric methods.[25]

All batch adsorption experiments were conducted in triplicate under identical conditions. The reported values represent the arithmetic mean ± standard deviation (mean ± SD). Standard deviation was calculated using:

$$\mathrm{SD} = \sqrt{\frac{\sum (x_i - \bar{x})^2}{n-1}} \quad (1)$$

where $\bar{x}$ is the mean value and $n = 3$. Reported uncertainties were rounded to two significant digits, and the mean values were rounded to the same decimal place as the corresponding standard deviation, in accordance with ISO/IEC Guide 98-3 (GUM:1995) recommendations for uncertainty reporting.

Post-desorption characterization will be performed to assess the structural integrity and stability of the regenerated adsorbents. XRD analysis will be conducted to detect any crystallinity changes while SEM will provide insights into morphological and elemental composition alterations. BET surface area analysis will determine whether repeated use affects porosity and adsorption capacity. FT-IR will also be utilized to examine changes in functional groups, helping to identify any surface modifications resulting from multiple adsorption–desorption cycles.[26]

The reusability of the adsorbents will be evaluated over 5–10 consecutive adsorption–desorption cycles. For each cycle, fluoride and phosphate removal efficiency will be measured, and the percentage retention of adsorption capacity will be calculated. A decline of less than 20% after multiple cycles will indicate good reusability, whereas a significant reduction in efficiency may suggest surface degradation or pore blockage. The regeneration performance of nickel-based nanoparticles will also be compared with other commonly used adsorbents such as activated alumina, biochar, hydroxyapatite, and metal oxides. This comparative analysis will consider factors such as adsorption capacity retention, desorption efficiency, material cost, and long-term stability.

3. Results and discussion

3.1. XRD analysis

Materials synthesized were analyzed using X-ray diffraction (XRD) to study their crystalline structure and phase composition, as depicted in Fig. 1. The diffraction pattern of the pristine kaolinite support (black curve) shows peaks associated with kaolinite that corroborate with JCPDS card no. 00-014-0164, therefore confirming its purity and crystalline structure.[1]

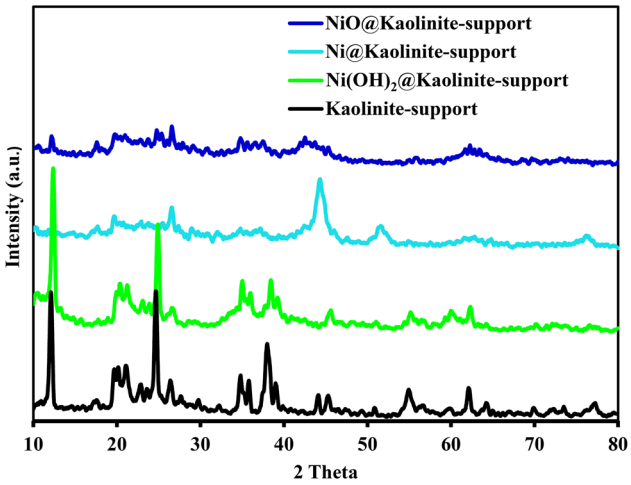

Fig. 1 XRD of kaolinite-supported, $Ni(OH)_2$@kaolinite-support, Ni@kaolinite-supported, and NiO@kaolinite-supported.

Distinct changes in the diffraction profiles were observed for the $Ni(OH)_2$@kaolinite-support sample (green curve) that exhibits distinctive reflections around $2\theta = 19.2°$, 33.1°, 38.5°, 52.1°, and 59.1°, which were associated with the standard diffraction peaks of brucite-type nickel hydroxide [JCPDS card no. 00-014-0117]. It could be concluded that the deposition of $Ni(OH)_2$ onto the kaolinite-support was successful.[27]

The alteration results in the Ni@kaolinite-support sample were achieved by reducing the $Ni(OH)_2$ modified support, where new reflections appeared at $2\theta = 44.5°$, 51.8°, and 76.4° which can be ascribed to (111), (200), and (220) planes of metallic Ni (face centered cubic, JCPDS card no. 00-004-0850), respectively.[28] This change confirms the assumption of synthesizing metallic nickel nanoparticles through thermal treatment or reduction as they exhaustively showed the $Ni(OH)_2$ peaks.

After calcination, the NiO@kaolinite-support composite (blue curve) was formed. The oxidation of metallic $Ni(OH)_2$ to NiO is confirmed by the distinctive peaks in the XRD pattern at $2\theta = 37.2°$, 43.3°, and 62.9°, which correspond to the (111), (200), and (220) planes of NiO (JCPDS card no. 00-047-1049).[11] These broad peaks indicate that the NiO crystallites are nanoscale in nature. The disappearance of the characteristic kaolinite peaks in the XRD patterns of NiO@kaolinite and Ni@kaolinite (compared to their presence in $Ni(OH)_2$@kaolinite) points to a significant structural transformation of the kaolinite support during the specific synthesis or post-treatment steps used to create the NiO and Ni phases. Kaolinite is thermally unstable. When heated to 500 °C, it undergoes an irreversible dehydroxylation reaction, losing its structural hydroxyl (OH) groups. This transforms the crystalline kaolinite into an amorphous, *meta*-kaolin phase ($Al_2Si_2O_7$) without sharp diffraction peaks. The long-range crystalline order of kaolinite is destroyed, so it's characteristic XRD peaks vanish. The remaining peaks would be solely from the newly formed crystalline NiO. So, the absence of kaolinite peaks in NiO and Ni samples is strong evidence that your preparation method involved a high-temperature step that decomposed the crystalline kaolinite into an amorphous material, which now acts as a different type of support (thermally activated aluminosilicate). In contrast, the low-temperature synthesis of the $Ni(OH)_2$ sample successfully preserved the original clay mineral structure.

3.2. FT-IR spectroscopy

FT-IR spectroscopy is a powerful analytical technique to predict synthesized materials molecular structure and composition, providing invaluable insights into their functional groups and chemical bonds. The FT-IR spectra of the kaolinite support and nickel-modified samples are presented in Fig. 2. The spectrum of pristine kaolinite displays characteristic bands associated with the kaolinite structure. The sharp peaks at 3650 cm^{-1} correspond to the O–H stretching vibrations of the inner surface hydroxyl groups of kaolinite. The band near 3620 cm^{-1} is attributed to inner hydroxyl stretching.[2] Furthermore, the band near 1110–1000 cm^{-1} is thought to be linked to Si–O bonds, while the peaks between 910 to 530 cm^{-1} suggest the presence of Al–O–H and Si–O–Al bonds, further demonstrating the structural form of the kaolinite.[29] Upon modification with $Ni(OH)_2$, dramatic changes are observed. Broadening of the O–H stretching region is indicative of increased hydrogen bonding, which shows the presence of nickel hydroxide species on the surface of kaolinite. New bands at 520–470 cm^{-1} are due to Ni–O vibrations, confirming the formation of $Ni(OH)_2$ on the support surface.[30] In the case of the Ni@kaolinite-support sample, a diminution of the intensity of hydroxyl stretching bands can result from partial dehydroxylation on reduction as well as free hydroxyl loss. Also, weakening or absence of features related to Ni–OH serves to indicate the reduction of $Ni(OH)_2$ to metallic Ni.[31]

In NiO@kaolinite-support material (blue curve), O–H stretching vibrations are weak and still evident, and additional bands at approximately 560 cm^{-1} appear, and can be ascribed to Ni–O stretching vibrations of NiO, indicative of successful

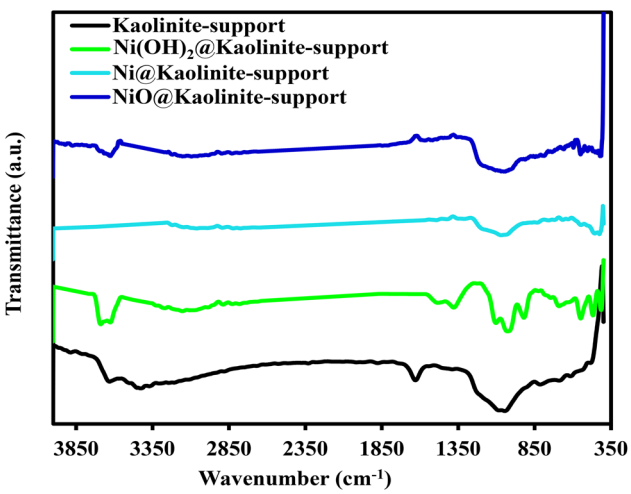

Fig. 2 FT-IR spectroscopy of kaolinite-support, $Ni(OH)_2$@kaolinite-supported, Ni@kaolinite-support, and NiO@kaolinite-support.

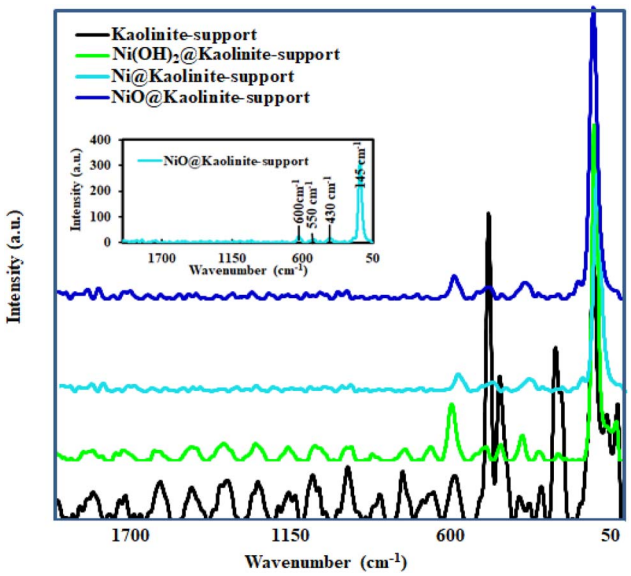

Fig. 3 Raman analysis of kaolinite-support, $Ni(OH)_2$@kaolinite-support, Ni@kaolinite-support, and NiO@kaolinite-support.

synthesis of NiO over kaolinite.[32,33] Overall, the FT-IR results complement the XRD findings, confirming the presence and transformation of nickel species and their interaction with the kaolinite support through structural and surface hydroxyl modifications.

3.3. Raman analysis

The Raman spectra of the $Ni(OH)_2$@kaolinite, Ni@kaolinite, and NiO@kaolinite composites are presented in Fig. 3 to provide insight into the vibrational properties and structural transformations of nickel species supported on kaolinite. The pristine kaolinite spectrum shows sharp and well-defined peaks, particularly in the regions around ~145, 207, 267, 356, 400, 466, 515, 694, and 755 cm^{-1}, which are characteristic of kaolinite's layered silicate structure.[3] These bands can be assigned to Al–O and Si–O bending and stretching vibrations, consistent with literature values.[33]

For the $Ni(OH)_2$@kaolinite sample, additional bands appear that are not present in the kaolinite spectrum. Notably, broad peaks centered around ~465 and 525 cm^{-1}, along with several features in the 100–400 cm^{-1} region, correspond to the vibrational modes of Ni–O and Ni–OH bonds, indicative of brucite-like $Ni(OH)_2$ structure. These peaks confirm the successful deposition of nickel hydroxide onto the kaolinite support.[34]

In the Ni@kaolinite sample (cyan curve), the characteristic $Ni(OH)_2$ bands are significantly suppressed or completely absent. This reduction of intensity confirms the decomposition of nickel hydroxide and the formation of metallic Ni. While metallic Ni itself is generally Raman inactive due to its centro-symmetric FCC structure, the diminished Ni–OH peaks corroborate the transformation upon reduction.[35]

The NiO@kaolinite composite displays a distinct and sharp for one-phonon F_{2g} mode of cubic NiO is typically reported (TO at 400–440 cm^{-1} and LO at 550 cm^{-1} modes). Accordingly, Fig. 3 shows a broad band centered around 550 cm^{-1} is observed, which corresponds to the characteristic F_{2g} mode of NiO, confirming the presence of crystalline nickel oxide.[36] This confirms the oxidation of nickel species to crystalline NiO. The absence of additional peaks in the NiO@kaolinite spectrum further supports the formation of pure NiO without residual hydroxide or metallic phases. Across all modified samples, the kaolinite peaks are retained with varying intensities, confirming that the support maintains its structural integrity during the deposition and transformation of the nickel species.[37] In summary, Raman spectra provide complementary evidence to XRD and FT-IR results, confirming the successful synthesis and phase transformation of nickel species ($Ni(OH)_2$ → Ni → NiO) supported on kaolinite.

3.4. BET analysis

The Brunauer–Emmett–Teller (BET) surface area analysis of the pristine kaolinite and nickel-modified composites $Ni(OH)_2$@-clay, NiO@clay, and Ni@clay reveals key insights into the structural modifications induced by nickel incorporation and their implications for adsorption performance as shown in Table 1. The pure kaolinite clay exhibited a high surface area of 140 $m^2\ g^{-1}$, consistent with its layered alumino-g silicate structure, which provides abundant active sites for adsorption. Upon functionalization with nickel species, a gradual decrease in surface area was observed as; $Ni(OH)_2$@clay (135 $m^2\ g^{-1}$) shows the slight reduction suggests that nickel hydroxide deposition partially occupies the clay's pores without significant structural disruption. NiO@clay (120 $m^2\ g^{-1}$) shows the further decrease indicates possible nanoparticle aggregation and pore blockage during thermal conversion of $Ni(OH)_2$ to NiO. While Ni@clay (115 $m^2\ g^{-1}$) shows the lowest surface area, observed for the metallic Ni-loaded clay, likely results from denser Ni nanoparticle formation and poor filling during reduction.[38] This trend (clay > $Ni(OH)_2$@clay > NiO@clay > Ni@clay) highlights that while nickel modification reduces surface area, the composites retain sufficient porosity (>115 $m^2\ g^{-1}$) for effective

Table 1 Physical adsorption properties of as-prepared materials (with error bars)

Sample	Surface area ($m^2\ g^{-1}$)	Pore volume ($cm^3\ g^{-1}$)	Average pore diameter (nm)
Clay	140 ± 5	0.25 ± 0.02	3.5 ± 0.1
Ni(OH)@clay	135 ± 4	0.22 ± 0.02	3.7 ± 0.1
NiO@clay	120 ± 3	0.18 ± 0.01	4.2 ± 0.2
Ni@clay	115 ± 3	0.15 ± 0.01	4.5 ± 0.2

adsorption. The retained surface area, combined with newly introduced active nickel sites, suggests a trade-off between textural properties and enhanced chemisorption capabilities.

Despite the reduced surface area, nickel-modified clays are expected to exhibit superior fluoride (F^-) and phosphate (PO_4^{3-}) adsorption due to:

- Enhanced chemisorption: $Ni(OH)_2$ and NiO provide hydroxyl groups and Lewis acid sites that strongly interact with anions.
- Electrostatic attraction: the positively charged nickel species at neutral pH improve anion uptake.
- Ligand exchange mechanisms: phosphate and fluoride may replace surface OH groups on nickel phases.

The higher fluoride/phosphate removal efficiency of $Ni(OH)_2$@clay and NiO@clay compared to pristine clay despite their lower surface area supports the dominance of chemical interactions over pure physical adsorption. The results concluded that; while nickel doping reduces kaolinite's surface area, the introduced active sites enhance specific surface interactions and ligand-exchange affinity toward fluoride and phosphate ions, making these composites highly effective for targeted anion removal. The balance between porosity and functionalization underscores their potential as multifunctional adsorbents for water treatment and resource recovery.[39]

3.5. SEM mapping-EDX analysis

To analyze the surface morphology and structural characteristics of the nanocomposites, scanning electron microscopy (SEM) was performed on the samples of $Ni(OH)_2$, NiO@kaolinite, and Ni@kaolinite. Fig. 4 shows distinct morphological differences that reflect the effect of nickel incorporation and subsequent oxidation processes on the kaolinite support.

The pristine $Ni(OH)_2$ sample shows a flaky, layered structure which suggests low crystallinity and high surface area morphology due to its poor crystallinity as well as abundant surface area.[40] On the other hand, the Ni@kaolinite composite shows the successful deposition of nickel species onto the surface of kaolinite.

Nickel particles, which appear in the form of small and semi-spherical aggregates, coat the kaolinite layers and are uniformly dispersed throughout. This disposition confirms that a strong linkage between Ni and the kaolinite support was formed, which is beneficial to the surface activity.[41]

For the NiO@kaolinite composite, SEM images display a more compact and granular morphology compared to Ni@kaolinite. Formation of NiO is likely to cause some sintering or cross junctioning of the particles during thermal treatment, which diminishes surface porosity but increases structural integrity of the particles.[18] The structure of kaolinite retains its identity, although less prominently because its edges have been softened and lowered because of the encasement and probable infiltration of NiO species.

The SEM analysis proved that Ni and NiO (NPs) supported on kaolinite were successfully synthesized while also depicting the morphological changes due to the conversion of hydroxide to oxide. Because of the changes in surface area, porosity, and the

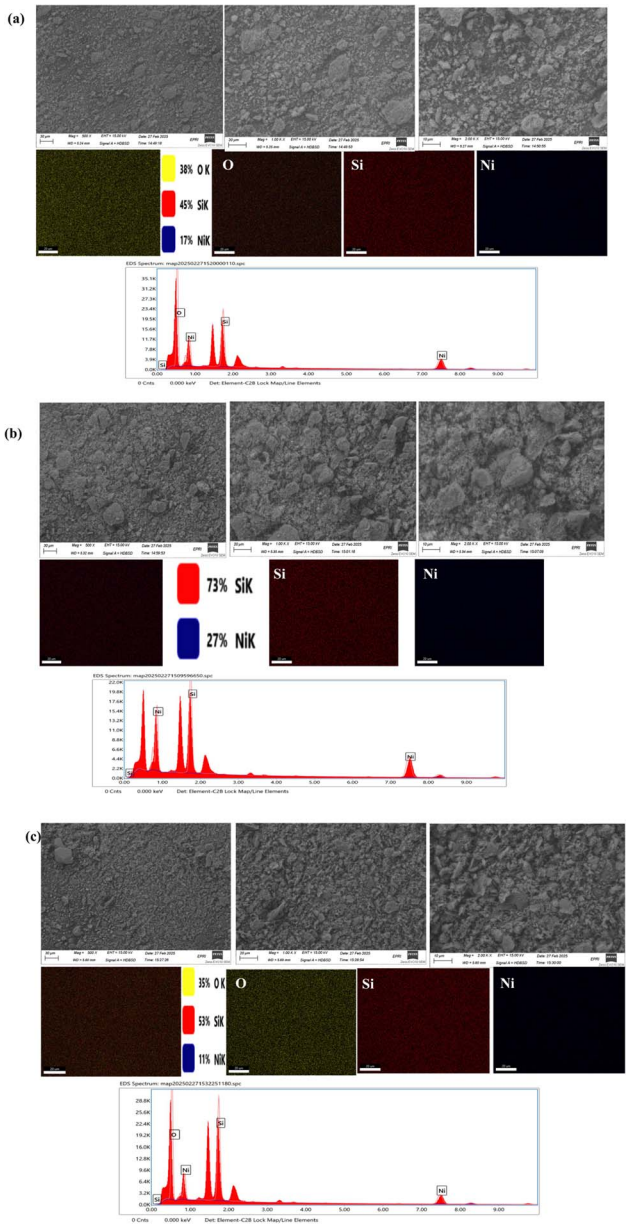

Fig. 4 SEM mapping-EDX of (a) $Ni(OH)_2$@kaolinite-support (b) Ni@kaolinite-support, and (c) NiO@kaolinite-support.

accessibility of active sites, these structural characteristics are vital in determining the performance of the composites as catalysts or adsorbents.

The elemental distribution and composition of the prepared nanocomposites were analyzed by energy-dispersive X-ray spectroscopy (EDX) mapping. For $Ni(OH)_2$@kaolinite-support, the maps show even distribution of nickel (Ni) signals over the kaolinite platelets separated by co-localized Si, Al and O signals, verifying that deposition of the nickel hydroxide phase does not destroy the clay sheet morphology. In contrast, the Ni@kaolinite-supported sample exhibits numerous Ni clusters with higher intensity of the metallic state that are related to high concentration appearing in the Si and Al maps (indicating a more amorphous or sintered aluminosilicate support) as

a result of reduction at high temperature which has produced metallic nickel and decomposed the crystalline kaolinite. The NiO@kaolinite-support maps show a homogeneous granular distribution of Ni and O throughout the support; whereas, Si and Al signals are spread out without clear platelet morphology, further confirming that kaolinite have been converted into amorphous *meta*-kaolin upon calcination with formation of well-dispersed NiO. Taken together, the EDX maps support the general phase transformations proposed by XRD: retention of kaolinite-like kaocuse-structure in the low temperature $Ni(OH)_2$ sample, loss of this (kaolinite) structure during the syntheses to produce NiO and/or Ni counterpart that exhibit significant variation in both nickel dispersion and oxidation state.

3.6. Dynamic light scattering (DLS) measurements

The particle size distribution and zeta potential of the synthesized nanomaterials were obtained using the Dynamic Light Scattering (DLS) with a laser angle 90° at 25 °C, (Zetasizer Nano-ZS90 instrument, Malvern Co., UK). The DLS is an instrument commonly used to assess the hydrodynamic diameter of nano particles based on the Brownian suspension movement of particles.[42] As shown in Fig. 5 and summarized in Table 2, the measurements provide insight into the colloidal stability and surface charge of the prepared samples: kaolinite, $Ni(OH)_2$, Ni@kaolinite, and NiO@kaolinite. The surface charge and possible stability of the suspended (NPs) are indicated by the zeta potential values. In accordance with its known anionic surface, pure kaolinite showed a negative zeta potential of −3.38 mV.[43] As a sign of positively charged hydroxide surfaces, $Ni(OH)_2$ showed a noticeably positive zeta potential of +21.3 mV.[44]

Table 2 Zeta potential of the prepared nanocomposites

Sample	Zeta potential (mV)
Kaolinite	−3.38 ± 0.10
$Ni(OH)_2$	21.3 ± 0.5
Ni@kaolinite	−3.24 ± 0.12
NiO@kaolinite	−3.12 ± 0.15

Both Ni@kaolinite (−3.24 mV) and NiO@kaolinite (−3.12 mV) maintained somewhat negative zeta potential values when added to the kaolinite support, although not as much as pure kaolinite. This implies electrostatic interaction or partial surface coverage between the nickel-based and kaolinite phases, which could affect the stability of the dispersion and the behavior of particle aggregation.[45] These interactions are further supported by the DLS size distribution patterns.

The qualitative DLS profiles most likely display differences in particle size and polydispersity, as shown in (Fig. 5). Larger hydrodynamic diameters are usually the consequence of aggregation or the creation of core–shell structures when metallic or oxide species, such as Ni and NiO, are present in a kaolinite support. The Ni@kaolinite and NiO@kaolinite samples' near-neutral zeta potential values also suggest less electrostatic repulsion, which could result in more particle agglomeration. Overall, the DLS data demonstrate that nickel incorporation into kaolinite alters the surface charge and likely

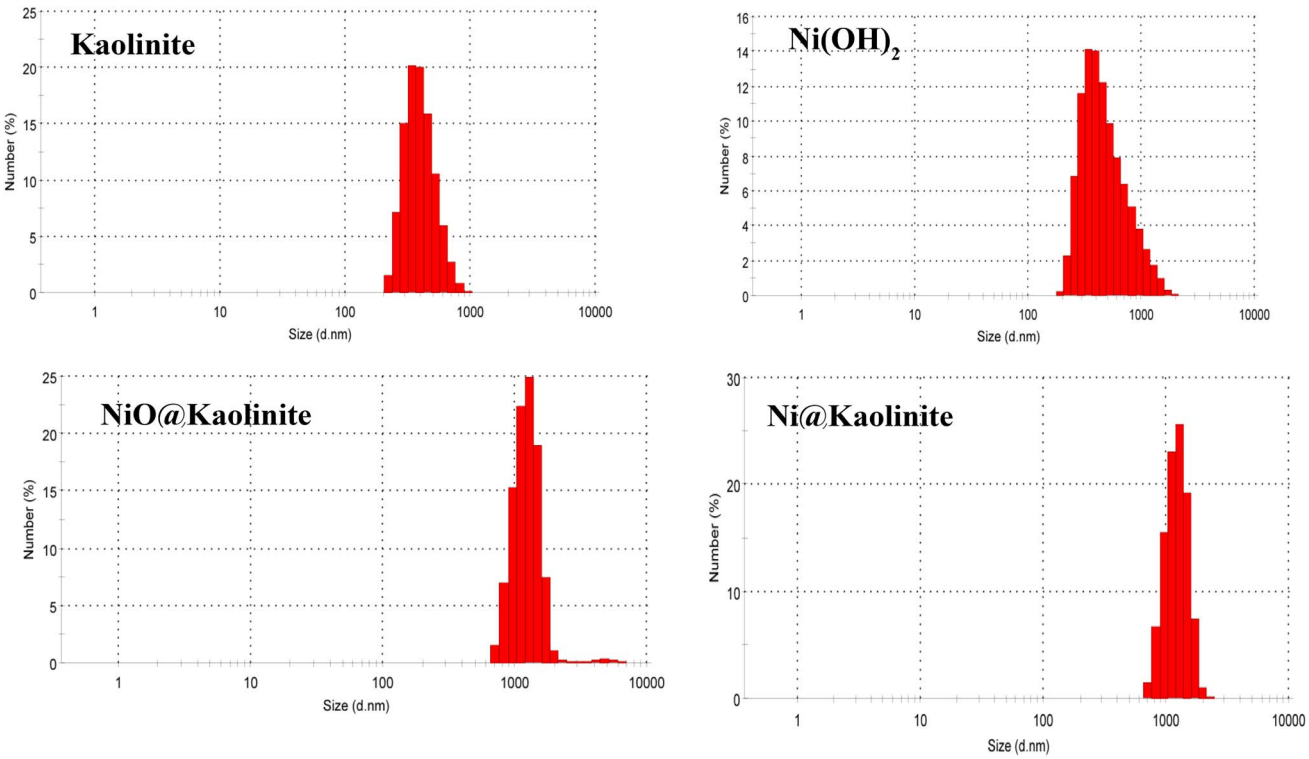

Fig. 5 DLS pattern of the prepared nanocomposites.

the size distribution of the resulting composites.[46] These changes can significantly impact their dispersion behavior and potential applications in catalysis or adsorption, where surface characteristics are critical.

3.7. Fluoride (F^-) adsorption study

3.7.1. Effect of initial fluoride concentration on adsorption capacity. The adsorption capacity (q_e) of Ni, NiO, and $Ni(OH)_2$ nanoparticles was evaluated at different initial fluoride concentrations ranging from 5 mg L^{-1} to 100 mg L^{-1}, as shown in Table 3 and Fig. 6. The results indicate that the adsorption capacity increases with increasing fluoride concentration, suggesting strong interaction between fluoride ions and the adsorbents.

At a lower initial fluoride concentration of 5 mg L^{-1}, the adsorption capacity was 4.2 mg g^{-1} for Ni, 4.5 mg g^{-1} for NiO, and 5.1 mg g^{-1} for $Ni(OH)_2$, achieving a high removal efficiency of 90%. As the initial fluoride concentration increased to 10 mg L^{-1}, the adsorption capacity nearly doubled, reaching 8.0, 8.6, and 9.4 mg g^{-1} for Ni, NiO, and $Ni(OH)_2$, respectively, with a removal efficiency of 85%. Further an increase in fluoride concentration to 25 mg L^{-1} and 50 mg L^{-1} increased adsorption capacity to 18.2–21.0 mg g^{-1} and 30.6–34.2 mg g^{-1}, respectively. However, the removal efficiency decreased, dropping from 80% at 25 mg L^{-1} to 75% at 50 mg L^{-1}. This decline suggests that the available adsorption sites become saturated at higher fluoride concentrations, limiting further fluoride uptake.

At the highest concentration of 100 mg L^{-1}, the adsorption capacities reached 48.7 mg g^{-1} for Ni, 50.3 mg g^{-1} for NiO, and 52.6 mg g^{-1} for $Ni(OH)_2$, but the removal efficiency further decreased to 70%. This reduction is likely due to competition among fluoride ions for the active adsorption sites and possible repulsion between adsorbed fluoride ions and those remaining in the solution. The results confirm that $Ni(OH)_2$ exhibits the highest adsorption capacity among the three adsorbents, followed by NiO and Ni. This can be attributed to the higher surface area and hydroxyl functional groups of $Ni(OH)_2$, which enhance fluoride affinity.

3.7.2. Effect of contact time on fluoride adsorption. The adsorption kinetics of fluoride onto Ni, NiO, and $Ni(OH)_2$ nanoparticles were analyzed over various contact times, ranging from 5 min to 120 min, as shown in Table 4 and Fig. 7. The results indicate that the adsorption capacity increases with time, reaching equilibrium within 60–120 min for all adsorbents.

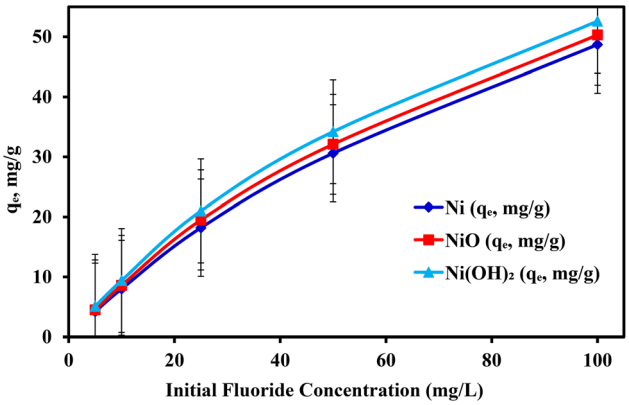

Fig. 6 Adsorption capacity (q_e) of Ni, NiO, and $Ni(OH)_2$ nanoparticles at different initial fluoride concentrations, error bars represent ±one standard deviation ($n = 3$).

At an initial contact time of 5 min, the adsorption capacities were 5.1 mg g^{-1} for Ni, 5.3 mg g^{-1} for NiO, and 6.0 mg g^{-1} for $Ni(OH)_2$, with a removal efficiency of 45%. This rapid initial uptake suggests that many active adsorption sites were available for fluoride binding. As the contact time increased to 15 min, the adsorption capacity nearly doubled, reaching 12.4 mg g^{-1} (Ni), 13.0 mg g^{-1} (NiO), and 14.5 mg g^{-1} $Ni(OH)_2$, with an improvement in removal efficiency to 60%. This phase represents the fast adsorption stage, where fluoride ions quickly occupy the readily available surface sites. By 30 min, the adsorption capacity further increased to 20.1 mg g^{-1} (Ni), 21.2 mg g^{-1} (NiO), and 23.5 mg g^{-1} $Ni(OH)_2$, with a removal efficiency of 75%, indicating continued but slightly slower adsorption as sites become occupied.

At 60 min, the adsorption process approached equilibrium, with adsorption capacities of 28.7 mg g^{-1} (Ni), 30.1 mg g^{-1} (NiO), and 32.6 mg g^{-1} $Ni(OH)_2$, corresponding to a high removal efficiency of 90%. Beyond this point, the adsorption rate slowed significantly as most active sites were saturated. At the final contact time of 120 min, a slight increase in adsorption capacity was observed (30.2 mg g^{-1} for Ni, 31.8 mg g^{-1} for NiO, and 34.3 mg g^{-1} for $Ni(OH)_2$), with a 95% removal efficiency. This suggests that adsorption equilibrium was reached, and no significant fluoride removal occurred beyond this time. The kinetic data were best fitted by the pseudo second order model based on correlation coefficients and error analysis. It is important to note that this model provides a mathematical

Table 3 Effect of initial fluoride concentration on adsorption capacity

Initial fluoride concentration (mg L^{-1})	Adsorption capacity (q_e, mg g^{-1}) – Ni	Adsorption capacity (q_e, mg g^{-1}) – NiO	Adsorption capacity (q_e, mg g^{-1}) – $Ni(OH)_2$	Removal efficiency (%)
5	4.2 ± 0.2	4.5 ± 0.2	5.1 ± 0.3	90 ± 2
10	8.0 ± 0.3	8.6 ± 0.3	9.4 ± 0.4	85 ± 2
25	18.2 ± 0.5	19.5 ± 0.6	21.0 ± 0.7	80 ± 3
50	30.6 ± 0.8	32.1 ± 0.9	34.2 ± 1.0	75 ± 3
100	48.7 ± 1.2	50.3 ± 1.3	52.6 ± 1.5	70 ± 4

Table 4 Effect of contact time on fluoride adsorption

Contact time (min)	Adsorption capacity (q_e, mg g^{-1}) – Ni	Adsorption capacity (q_e, mg g^{-1}) – NiO	Adsorption capacity (q_e, mg g^{-1}) – $Ni(OH)_2$	Removal efficiency (%)
5	5.1 ± 0.2	5.3 ± 0.2	6.0 ± 0.3	45 ± 2
15	12.4 ± 0.4	13.0 ± 0.5	14.5 ± 0.6	60 ± 2
30	20.1 ± 0.6	21.2 ± 0.7	23.5 ± 0.8	75 ± 3
60	28.7 ± 0.9	30.1 ± 1.0	32.6 ± 1.1	90 ± 3
120	30.2 ± 1.0	31.8 ± 1.2	34.3 ± 1.3	

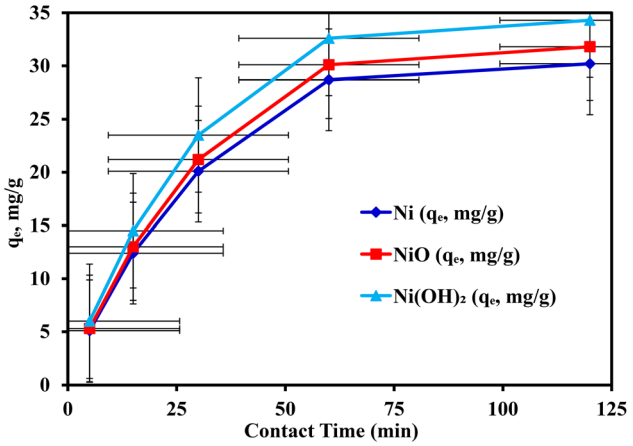

Fig. 7 Fluoride adsorption kinetics over time, error bars represent ±one standard deviation ($n = 3$).

description of adsorption rate behavior and does not by itself confirm a chemisorption mechanism.

Therefore, additional diffusion and thermodynamic analyses were used to interpret the adsorption mechanism. $Ni(OH)_2$ again demonstrated the highest adsorption capacity among the three adsorbents, likely due to its higher surface area and enhanced fluoride-binding interactions.

It should be emphasized that kinetic model fitting alone cannot be used to distinguish between physisorption and chemisorption mechanisms. The pseudo second order model is widely applied because of its strong empirical fitting performance across many adsorption systems, including those

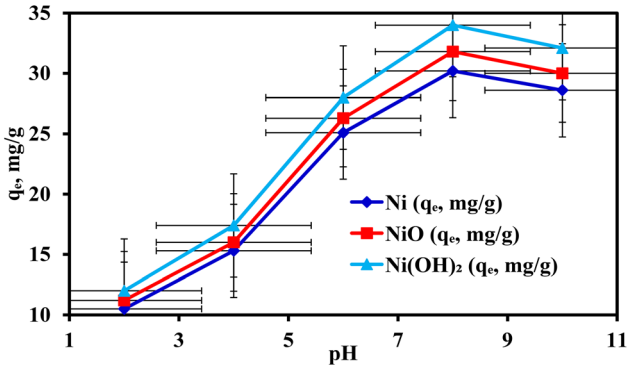

Fig. 8 Variation in fluoride adsorption efficiency at different pH values, error bars represent ±one standard deviation ($n = 3$).

controlled by surface reaction, film diffusion, or intra-particle diffusion. Therefore, mechanistic interpretation in this study was based on combined evidence from pH dependence, surface chemistry, diffusion modeling, and thermodynamic parameters rather than kinetic fitting alone.

3.7.3. Effect of pH on fluoride adsorption. Fluoride adsorption onto Ni, NiO, and $Ni(OH)_2$ nanoparticles was studied at different pH levels ranging from 2 to 10, as shown in Fig. 8. The results demonstrate a strong dependency of fluoride removal on the solution pH, highlighting the role of surface charge and ion–exchange interactions in the adsorption mechanism. At an acidic pH of 2, the adsorption capacities were 10.5 mg g^{-1} for Ni, 11.2 mg g^{-1} for NiO, and 12.0 mg g^{-1} for $Ni(OH)_2$, corresponding to a fluoride removal efficiency of 55%. The lower adsorption at this pH can be attributed to excess hydrogen ions (H^+), which compete with fluoride (F^-) for active adsorption sites on the nanoparticle surfaces.

As the pH increased to 4, the adsorption capacity improved significantly, reaching 15.3 mg g^{-1} (Ni), 16.0 mg g^{-1} (NiO), and 17.4 mg g^{-1} $Ni(OH)_2$, with a removal efficiency of 65%. This suggests that the adsorbent surfaces were becoming more negatively charged, enhancing electrostatic attraction between fluoride anions and the positively charged active sites. At a neutral pH of 6, maximum adsorption was observed, with capacities of 25.1 mg g^{-1} (Ni), 26.3 mg g^{-1} (NiO), and 28.0 mg g^{-1} $Ni(OH)_2$, achieving a removal efficiency of 80%. This can be attributed to optimal electrostatic interactions, where the adsorbent surface retains a partial positive charge, facilitating strong fluoride binding.[47]

The highest fluoride adsorption occurred at a slightly alkaline pH of 8, where adsorption capacities reached 30.2 mg g^{-1} (Ni), 31.8 mg g^{-1} (NiO), and 34.0 mg g^{-1} $Ni(OH)_2$, with a removal efficiency of 90%. At this pH, the adsorbent surfaces were still positively charged enough to attract fluoride ions, while there was minimal competition from hydroxide ions (OH^-). Beyond pH 10, a slight decline in adsorption was observed, with capacities decreasing to 28.6 mg g^{-1} (Ni), 30.0 mg g^{-1} (NiO), and 32.1 mg g^{-1} $Ni(OH)_2$, and removal efficiency dropping to 85%. This reduction is likely due to increased competition between fluoride (F^-) and hydroxide (OH^-) ions, as both anions have similar affinities for the adsorption sites. The overall trend indicates that pH 6–8 is the optimal range for fluoride removal, where electrostatic attraction and ion exchange mechanisms are most effective. The higher adsorption capacity of $Ni(OH)_2$ compared to Ni and NiO further confirms its superior fluoride-binding ability, possibly

due to its surface hydroxyl groups facilitating stronger interactions with fluoride ions.

3.8. Phosphate (PO_4^{3-}) adsorption study

3.8.1. Effect of initial phosphate (PO_4^{3-}) concentration on adsorption capacity. The adsorption capacity (q_e) of Ni, NiO, and $Ni(OH)_2$ nanoparticles was evaluated at different initial phosphate concentrations ranging from 5 to 100 mg L^{-1}, as shown in Fig. 9. The results indicate that adsorption capacity increases with increasing phosphate concentration, although the removal efficiency decreases at higher concentrations due to site saturation. At a low initial phosphate concentration of 5 mg L^{-1}, the adsorption capacity was 4.8 mg g^{-1} for Ni, 5.2 mg g^{-1} for NiO, and 5.8 mg g^{-1} for $Ni(OH)_2$, with a removal efficiency of 92%. This suggests that most of the phosphate ions are effectively captured by the abundant active adsorption sites at lower concentrations.

When the initial phosphate concentration increased to 10 mg L^{-1}, the adsorption capacity nearly doubled, reaching 9.1 mg g^{-1} (Ni), 9.8 mg g^{-1} (NiO), and 10.6 mg g^{-1} $Ni(OH)_2$. However, the removal efficiency slightly decreased to 88%. This indicates that more phosphate ions were available for adsorption, but competition for binding sites started to occur. At 25 mg L^{-1}, the adsorption capacity further increased to 20.5 mg g^{-1} (Ni), 21.8 mg g^{-1} (NiO), and 23.4 mg g^{-1} $Ni(OH)_2$, but the removal efficiency dropped to 82%. This reduction is attributed to site saturation, where some phosphate ions remain in the solution after reaching equilibrium.

At 50 mg L^{-1}, the adsorption capacities reached 33.4 mg g^{-1} (Ni), 35.0 mg g^{-1} (NiO), and 37.5 mg g^{-1} $Ni(OH)_2$, with a further decline in removal efficiency to 78%. The trend suggests that although the adsorbents continue to take up phosphate, their capacity to eradicate it diminishes as surface sites become increasingly occupied. At the highest concentration of 100 mg L^{-1}, the maximum adsorption capacities observed were 50.3 mg g^{-1} (Ni), 52.1 mg g^{-1} (NiO), and 55.0 mg g^{-1} $Ni(OH)_2$, with the lowest removal efficiency of 70%. This decline confirms that competition among phosphate ions for limited adsorption sites at high phosphate concentrations leads to reduced efficiency. Among the three adsorbents, $Ni(OH)_2$ consistently exhibited the highest adsorption capacity, followed by NiO and Ni. The superior performance of $Ni(OH)_2$ is likely due to its enhanced surface hydroxyl groups, which facilitate stronger electrostatic interactions and ligand exchange mechanisms with phosphate ions. These findings suggest that Ni, NiO, and $Ni(OH)_2$ nanoparticles can effectively remove phosphate from aqueous solutions, especially at moderate concentrations (5–25 mg L^{-1}). However, adsorption site saturation limits removal efficiency at higher phosphate levels, highlighting the importance of optimizing dosage and regeneration cycles for practical applications.

3.8.2. Effect of pH on phosphate (PO_4^{3-}) adsorption. Phosphate adsorption onto Ni, NiO, and $Ni(OH)_2$ nanoparticles was studied at different pH levels ranging from 2 to 10, as shown in Fig. 10. The results indicate that phosphate adsorption is highly pH-dependent and influenced by the surface charge of the adsorbents and the speciation of phosphate in the solution. At a strongly acidic pH of 2, the adsorption capacities were relatively low, measuring 9.2 mg g^{-1} for Ni, 9.8 mg g^{-1} for NiO, and 10.5 mg g^{-1} for $Ni(OH)_2$, with a removal efficiency of 50%. The lower adsorption at this pH is attributed to the high concentration of hydrogen ions (H^+), which compete with phosphate anions for available adsorption sites. Additionally, at very low pH, phosphate exists mainly in the form of H_3PO_4, which has a weaker electrostatic interaction with the adsorbent surfaces.[48]

As the pH increased to 4, a significant improvement in adsorption was observed, with adsorption capacities rising to 17.4 mg g^{-1} (Ni), 18.2 mg g^{-1} (NiO), and 19.6 mg g^{-1} ($Ni(OH)_2$), achieving a removal efficiency of 68%. This increase is due to the presence of $H_2PO_4^-$ ions, which have a stronger affinity for the positively charged adsorption sites. The highest phosphate adsorption occurred at a pH range of 6–8, where adsorption capacities reached 30.5 mg g^{-1} (Ni), 32.1 mg g^{-1} (NiO), and 34.7 mg g^{-1} ($Ni(OH)_2$), with a removal efficiency of 88–92%. At this pH range, phosphate exists primarily as $H_2PO_4^-$ and HPO_4^{2-}, which strongly interact with the metal hydroxide surfaces through electrostatic attraction and ligand exchange mechanisms. The high adsorption efficiency in this range confirms that $Ni(OH)_2$ exhibits the best phosphate removal

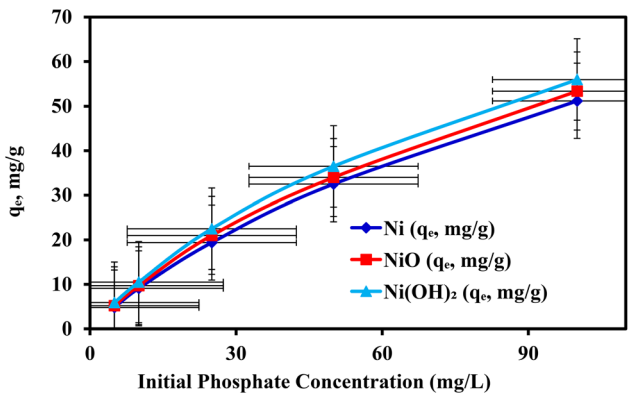

Fig. 9 Adsorption capacity (q_e) of Ni, NiO, and $Ni(OH)_2$ nanoparticles at different initial phosphate concentrations, error bars represent ±one standard deviation ($n = 3$).

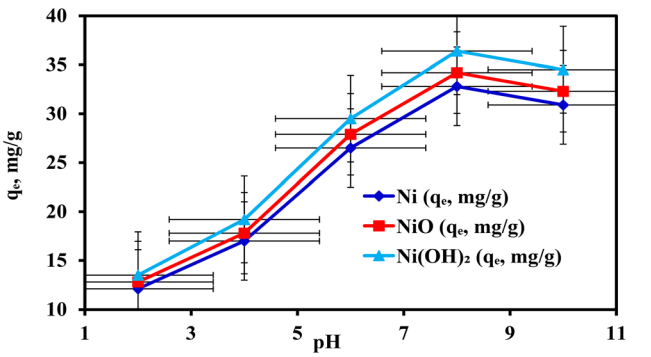

Fig. 10 Variation in phosphate adsorption efficiency at different pH values, error bars represent ±one standard deviation ($n = 3$).

Table 5 Regeneration cycles for fluoride adsorption efficiency (q_e, mg g^{-1})

Cycle no.	Ni (q_e, mg g^{-1})	Retention (%)	NiO (q_e, mg g^{-1})	Retention (%)	$Ni(OH)_2$ (q_e, mg g^{-1})	Retention (%)
1	30.2 ± 0.8	100 ± 2	31.8 ± 0.9	100 ± 2	34.3 ± 1.0	100 ± 2
2	28.9 ± 0.7	96 ± 2	30.5 ± 0.8	96 ± 2	32.8 ± 0.9	96 ± 2
3	27.1 ± 0.7	90 ± 3	29.3 ± 0.8	92 ± 3	31.1 ± 0.9	91 ± 3
4	26.0 ± 0.6	86 ± 3	28.1 ± 0.7	88 ± 3	30.0 ± 0.8	87 ± 3
5	25.4 ± 0.6	84 ± 3	27.0 ± 0.7	85 ± 3	29.3 ± 0.8	85 ± 3
6	24.0 ± 0.6	79 ± 4	25.5 ± 0.7	80 ± 4	28.0 ± 0.8	82 ± 4
7	23.2 ± 0.5	77 ± 4	24.9 ± 0.6	78 ± 4	27.0 ± 0.7	79 ± 4
8	22.5 ± 0.5	75 ± 4	24.3 ± 0.6	76 ± 4	26.5 ± 0.7	77 ± 4
9	21.8 ± 0.5	72 ± 5	24.0 ± 0.6	75 ± 4	26.4 ± 0.7	77 ± 4
10	21.5 ± 0.5	71 ± 5	23.8 ± 0.6	75 ± 4	26.2 ± 0.7	76 ± 4

performance, likely due to its abundant hydroxyl groups that facilitate effective phosphate binding.

Beyond pH 8, the adsorption capacity declined slightly, with capacities of 28.2 mg g^{-1} (Ni), 29.8 mg g^{-1} (NiO), and 32.0 mg g^{-1} $Ni(OH)_2$ at pH 10, leading to a removal efficiency of 85%. This reduction is attributed to the increased competition from hydroxide ions (OH^-), which can occupy active adsorption sites and reduce phosphate retention. At higher pH values, phosphate exists mainly in the form of PO_4^{3-}, which experiences greater electrostatic repulsion from the negatively charged adsorbent surfaces, further limiting adsorption efficiency.

3.9. Regeneration and reusability studies

The sustainability of Ni, NiO, and $Ni(OH)_2$ nanoparticles as adsorbents for fluoride and phosphate removal was evaluated over multiple regeneration cycles, as shown in Tables 5 (fluoride) and 6 (phosphate), with Fig. 11 and 12. The results indicate a gradual decrease in adsorption capacity with increasing cycles, although the adsorbents retained significant efficiency even after ten regeneration cycles.

The initial adsorption capacities were 30.2 mg g^{-1} (Ni), 31.8 mg g^{-1} (NiO), and 34.3 mg g^{-1} $Ni(OH)_2$ in the first cycle, with 100% adsorption retention. After the second and third regeneration cycles, adsorption capacity slightly decreased, with $Ni(OH)_2$ maintaining the highest efficiency at 32.8 mg g^{-1} (cycle 2) and 31.1 mg g^{-1} (cycle 3), corresponding to 95% and 90% adsorption retention, respectively. By the fifth cycle, adsorption capacities further declined to 25.4 mg g^{-1} (Ni), 27.0 mg g^{-1} (NiO), and 29.3 mg g^{-1} $Ni(OH)_2$, with adsorption retention of 85%, indicating a steady but controlled loss of efficiency due to possible fouling or minor structural degradation.

At the tenth cycle, the adsorption capacity was reduced to 21.5 mg g^{-1} (Ni), 23.8 mg g^{-1} (NiO), and 26.2 mg g^{-1} $Ni(OH)_2$, with adsorption retention dropping to 75%. Despite this decline, the nanoparticles exhibited reasonable efficiency, confirming their suitability for multiple reuse cycles. The reduction in performance is likely attributed to residual fluoride ions blocking active sites, partial dissolution of metal oxides, or minor changes in surface chemistry.

The phosphate adsorption study followed a similar trend, with the highest initial adsorption capacities of 32.0 mg g^{-1}

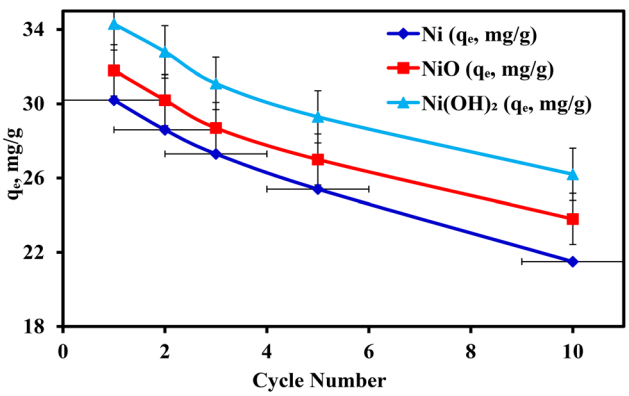

Fig. 11 Fluoride adsorption efficiency over multiple regeneration cycles, error bars represent ±one standard deviation ($n = 3$).

Table 6 Regeneration cycles for phosphate adsorption efficiency (q_e, mg g^{-1})

Cycle no.	Ni (q_e, mg g^{-1})	Retention (%)	NiO (q_e, mg g^{-1})	Retention (%)	$Ni(OH)_2$ (q_e, mg g^{-1})	Retention (%)
1	32.0 ± 0.8	100 ± 2	34.0 ± 0.9	100 ± 2	36.2 ± 1.0	100 ± 2
2	30.5 ± 0.7	95 ± 2	32.5 ± 0.8	96 ± 2	34.8 ± 0.9	96 ± 2
3	29.6 ± 0.7	92 ± 3	31.7 ± 0.8	93 ± 3	33.5 ± 0.9	93 ± 3
4	28.2 ± 0.6	88 ± 3	30.5 ± 0.7	90 ± 3	32.4 ± 0.8	90 ± 3
5	27.6 ± 0.6	86 ± 3	29.8 ± 0.7	88 ± 3	31.5 ± 0.8	87 ± 3
6	26.8 ± 0.6	84 ± 4	29.0 ± 0.7	85 ± 4	30.7 ± 0.8	85 ± 4
7	25.6 ± 0.6	80 ± 4	28.0 ± 0.7	82 ± 4	30.0 ± 0.8	83 ± 4
8	24.8 ± 0.5	78 ± 4	27.3 ± 0.6	80 ± 4	29.6 ± 0.7	82 ± 4
9	24.5 ± 0.5	77 ± 5	27.0 ± 0.6	79 ± 4	29.2 ± 0.7	81 ± 4
10	24.3 ± 0.5	76 ± 5	26.8 ± 0.6	79 ± 4	29.0 ± 0.7	80 ± 4

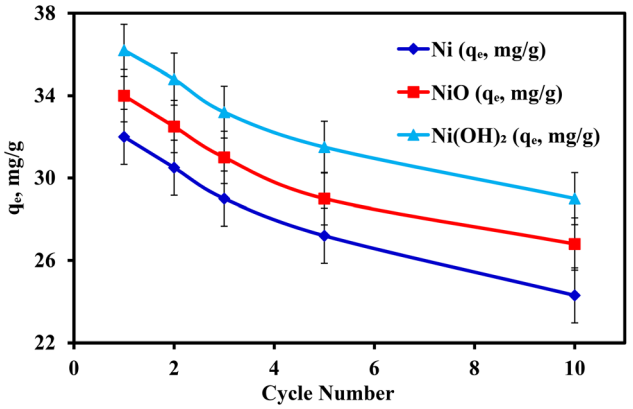

Fig. 12 Phosphate adsorption efficiency over multiple regeneration cycles, error bars represent ±one standard deviation ($n = 3$).

(Ni), 34.0 mg g^{-1} (NiO), and 36.2 mg g^{-1} $Ni(OH)_2$ at 100% adsorption retention in the first cycle. By the second cycle, adsorption capacities declined slightly to 30.5 mg g^{-1} (Ni), 32.5 mg g^{-1} (NiO), and 34.8 mg g^{-1} ($Ni(OH)_2$), with 96% retention, demonstrating that the adsorbents maintained high efficiency after regeneration.[49]

In the third and fifth cycles, adsorption capacity decreased gradually, reaching 31.5 mg g^{-1} for $Ni(OH)_2$ at cycle 5, with adsorption retention of 87%, which remains highly effective. After ten cycles, the adsorption capacity further declined to 24.3 mg g^{-1} (Ni), 26.8 mg g^{-1} (NiO), and 29.0 mg g^{-1} $Ni(OH)_2$, with a final retention of 78%. This trend suggests that the adsorbents remained functional even after prolonged reuse, making them viable for practical wastewater treatment applications.

3.10. Adsorption kinetics modeling

To elucidate the adsorption mechanisms and rate-controlling steps, experimental kinetic data were fitted to pseudo first order, pseudo second order, and intra-particle diffusion models. The kinetic parameters were determined from the linearized forms of these models and are presented in Tables 7–9 for fluoride and phosphate adsorption.

3.10.1. Pseudo first order kinetic model. The pseudo first order model, based on Lagergren's equation, assumes that the rate of adsorption is proportional to the number of unoccupied sites. The linearized form is expressed as:

$$\log(q_e - q_t) = \log q_e - \frac{k_1}{2.303} t \quad (2)$$

where q_e and q_t are the adsorption capacities (mg g^{-1}) at equilibrium and time t (min), respectively, and k_1 is the pseudo first order rate constant (min^{-1}). The parameters obtained from the linearized plots are summarized in Table 7.

The pseudo first order model showed moderate correlation coefficients ($R^2 = 0.902–0.931$), with calculated q_e values deviating significantly from experimental values. The higher χ^2 values (2.45–3.87) indicate poor fit, suggesting that the adsorption process does not follow first-order kinetics. This deviation implies that the rate is not solely dependent on the concentration of available sites.

3.10.2. Pseudo second order kinetic model. The pseudo second order model assumes that chemisorption or surface reactions control the adsorption rate. The linearized form is:

$$\frac{t}{q_t} = \frac{1}{k_2 q_e^2} + \frac{t}{q_e} \quad (3)$$

where k_2 is the pseudo second order rate constant (g mg^{-1} min^{-1}). The initial adsorption rate h_0 (mg g^{-1} min^{-1}) can be calculated as $h_0 = k_2 q_e^2$. The kinetic parameters are presented in Table 8 for both fluoride and phosphate adsorption.

The pseudo second order model demonstrated excellent fit to the experimental data, with high correlation coefficients ($R^2 > 0.989$) and low χ^2 values (0.08–0.18). The close agreement between experimental and calculated q_e values confirms that this model accurately describes the adsorption kinetics. The initial adsorption rates (h_0) increased in the order: Ni@kaolinite < NiO@kaolinite < $Ni(OH)_2$@kaolinite, indicating that $Ni(OH)_2$@kaolinite exhibits the fastest initial uptake rate. However, it is important to note that the pseudo second order model provides a mathematical description of the rate behavior and does not by itself confirm a specific adsorption mechanism. The model's success in fitting the data indicates that the adsorption rate is proportional to the square of the number of unoccupied sites, which is consistent with various mechanisms including surface complexation, electrostatic attraction, and ligand exchange. Therefore, additional thermodynamic and diffusion analyses are necessary to fully characterize the adsorption mechanism (see Sections 3.11 and 3.12).

3.10.3. Intra-particle diffusion model. The Weber–Morris intra-particle diffusion model was applied to identify the rate-limiting step. The model is expressed as:

$$q_t = k_{ip} t^{0.5} + C \quad (4)$$

where k_{ip} is the intra-particle diffusion rate constant (mg g^{-1} $min^{-0.5}$) and C is the intercept related to boundary layer thickness. If intra-particle diffusion is the sole rate-limiting step, the plot of q_t *vs.* $t^{0.5}$ should be linear and pass through

Table 7 Pseudo first order kinetic parameters for fluoride adsorption

Adsorbent	$q_{e,exp.}$ (mg g^{-1})	$q_{e,calc.}$ (mg g^{-1})	k_1 (min^{-1})	R^2	χ^2
Ni@kaolinite	30.2 ± 0.8	27.8 ± 1.2	0.031 ± 0.003	0.931	2.45
NiO@kaolinite	31.8 ± 0.7	29.1 ± 1.1	0.028 ± 0.002	0.918	3.12
$Ni(OH)_2$@kaolinite	34.3 ± 0.9	31.5 ± 1.3	0.025 ± 0.003	0.902	3.87

Table 8 Pseudo second order kinetic parameters for fluoride and phosphate adsorption

Adsorbent	Ion	$q_{e,exp.}$ (mg g^{-1})	$q_{e,calc.}$ (mg g^{-1})	k_2 (g mg^{-1} min^{-1})	h_0 (mg g^{-1} min^{-1})	R^2	χ^2
Ni@kaolinite	F^-	30.2 ± 0.8	30.6 ± 0.5	0.0032 ± 0.0002	2.99	0.991	0.15
Ni@kaolinite	PO_4^{3-}	32.0 ± 0.9	32.4 ± 0.6	0.0028 ± 0.0003	2.94	0.989	0.18
NiO@kaolinite	F^-	31.8 ± 0.7	32.4 ± 0.4	0.0039 ± 0.0003	4.09	0.994	0.12
NiO@kaolinite	PO_4^{3-}	34.0 ± 0.8	34.6 ± 0.5	0.0035 ± 0.0002	4.19	0.992	0.14
$Ni(OH)_2$@kaolinite	F^-	34.3 ± 0.9	34.9 ± 0.4	0.0046 ± 0.0004	5.60	0.996	0.08
$Ni(OH)_2$@kaolinite	PO_4^{3-}	36.2 ± 1.0	37.1 ± 0.5	0.0042 ± 0.0003	5.77	0.995	0.10

the origin ($C = 0$). The parameters for fluoride adsorption are presented in Table 9.

The intra-particle diffusion plots exhibited three distinct linear regions, indicating a multi-stage adsorption process. Stage 1 (high k_{ip1} values) represents rapid external surface adsorption and film diffusion. Stage 2 (moderate k_{ip2} values) corresponds to gradual intra-particle diffusion into pores. Stage 3 (low k_{ip3} values) represents the final equilibrium stage where adsorption rate slows due to decreased driving force. Importantly, the non-zero intercept values ($C > 0$) confirm that intra-particle diffusion is not the sole rate-controlling step. Instead, both surface adsorption and pore diffusion contribute to the overall adsorption process. The higher C values for $Ni(OH)_2$@-kaolinite indicate a greater contribution from boundary layer diffusion, which is consistent with its enhanced surface chemistry.

3.11. Thermodynamic analysis

Thermodynamic parameters, including Gibbs free energy change ($\Delta G°$), enthalpy change ($\Delta H°$), and entropy change ($\Delta S°$), were calculated to understand the spontaneity, heat changes, and randomness associated with the adsorption process. These parameters were determined using the van 't Hoff equation:

$$\ln K_e^\circ = -\frac{\Delta H^\circ}{RT} + \frac{\Delta S^\circ}{R} \quad (5)$$

$$\Delta G^\circ = -RT \ln K_e^\circ = \Delta H^\circ - T\Delta S^\circ \quad (6)$$

where, R is the universal gas constant (8.314 J mol^{-1} K^{-1}), T is the absolute temperature (K), and K_e° is the dimensionless equilibrium constant. To ensure thermodynamic validity, the Langmuir constant (K_L, in L mg^{-1}) was converted to a dimensionless standard equilibrium constant:

$$K_e^\circ = \frac{1000 \times K_L \times M_w \times C^\circ}{\gamma} \quad (7)$$

where M_w is the molecular weight of the adsorbate (g mol^{-1}), $C°$ is the standard concentration (1 mol L^{-1}), and γ is the activity coefficient (assumed $\approx$ 1 for dilute aqueous systems). The factor 1000 ensures unit consistency between mg and g. This approach avoids the incorrect use of the 55.51 mol L^{-1} water concentration factor, which is not applicable for adsorption equilibrium constants (Table 10).

The dimensionless equilibrium constant K_e° increased with temperature for both fluoride and phosphate, indicating enhanced adsorption at higher temperatures. This trend is characteristic of endothermic adsorption processes. The calculated thermodynamic parameters are presented in Table 11.

The negative $\Delta G°$ values at all temperatures confirm that the adsorption of fluoride and phosphate onto $Ni(OH)_2$@kaolinite is thermodynamically spontaneous and favorable. The magnitude of $\Delta G°$ became more negative with increasing temperature, indicating greater spontaneity at higher temperatures. The positive $\Delta H°$ values (24.6 kJ mol^{-1} for fluoride and 31.8 kJ mol^{-1} for phosphate) confirm that the adsorption process is endothermic, requiring energy input to proceed. These $\Delta H°$ values fall within the typical range of physical adsorption and surface complexation processes (<40 kJ mol^{-1}), which distinguishes

Table 10 Conversion of Langmuir constant to dimensionless equilibrium constant

Adsorbate	T (K)	K_L (L mg^{-1})	M_w (g mol^{-1})	K_e° (dimensionless)
Fluoride	298	0.082 ± 0.005	19.00	1558
Fluoride	308	0.094 ± 0.006	19.00	1786
Fluoride	318	0.109 ± 0.007	19.00	2071
Fluoride	328	0.128 ± 0.008	19.00	2432
Phosphate	298	0.065 ± 0.004	94.97	6173
Phosphate	308	0.072 ± 0.005	94.97	6838
Phosphate	318	0.081 ± 0.006	94.97	7693
Phosphate	328	0.093 ± 0.007	94.97	8832

Table 9 Intra-particle diffusion model parameters for fluoride adsorption

	Stage 1			Stage 2			Stage 3		
Adsorbent	k_{ip1}	C_1	R^2	k_{ip2}	C_2	R^2	k_{ip3}	C_3	R^2
Ni@kaolinite	3.85	2.14	0.985	1.42	12.8	0.962	0.28	26.5	0.891
NiO@kaolinite	4.12	1.87	0.988	1.56	13.5	0.971	0.31	28.2	0.903
$Ni(OH)_2$@kaolinite	4.58	1.52	0.992	1.78	14.2	0.978	0.35	30.8	0.912

Table 11 Thermodynamic parameters for fluoride and phosphate adsorption on $Ni(OH)_2$@kaolinite

Adsorbate	$\Delta H°$ (kJ mol^{-1})	$\Delta S°$ (J mol^{-1} K^{-1})	$\Delta G°_{298}$ (kJ mol^{-1})	$\Delta G°_{308}$ (kJ mol^{-1})	$\Delta G°_{318}$ (kJ mol^{-1})	$\Delta G°_{328}$ (kJ mol^{-1})
Fluoride	24.6 ± 1.8	96 ± 5	−4.0	−5.0	−5.9	−6.9
Phosphate	31.8 ± 2.1	112 ± 6	−1.6	−2.7	−3.9	−5.0

Table 12 Langmuir isotherm parameters for fluoride and phosphate adsorption

Adsorbent	Ion	q_{max} (mg g^{-1})	K_L (L mg^{-1})	R_L	R^2	χ^2
Ni@kaolinite	F^-	52.4 ± 2.1	0.068 ± 0.005	0.128–0.746	0.987	0.82
Ni@kaolinite	PO_4^{3-}	54.8 ± 2.3	0.053 ± 0.004	0.159–0.790	0.983	1.05
NiO@kaolinite	F^-	55.9 ± 2.0	0.075 ± 0.006	0.118–0.727	0.991	0.65
NiO@kaolinite	PO_4^{3-}	58.2 ± 2.2	0.061 ± 0.005	0.141–0.766	0.988	0.78
$Ni(OH)_2$@kaolinite	F^-	58.6 ± 1.8	0.082 ± 0.006	0.109–0.709	0.994	0.45
$Ni(OH)_2$@kaolinite	PO_4^{3-}	62.1 ± 2.0	0.069 ± 0.005	0.126–0.744	0.992	0.58

them from strong chemisorption processes that typically exhibit $\Delta H° > 80$ kJ mol^{-1}. Therefore, the adsorption mechanism cannot be classified as chemisorption based on thermodynamic magnitude alone. Instead, the process is attributed to a combination of electrostatic attraction, ligand exchange, and outer-sphere/inner-sphere surface complexation mechanisms. The positive $\Delta S°$ values (96 J mol^{-1} K^{-1} for fluoride and 112 J mol^{-1} K^{-1} for phosphate) indicate increased randomness at the solid–solution interface during adsorption. This entropy increase is attributed to the release of water molecules and counter-ions from the adsorbent surface upon fluoride and phosphate binding, resulting in a net increase in system disorder. The favorable entropy change further supports the spontaneous nature of the adsorption process.[45]

3.12. Adsorption isotherm modeling

Adsorption isotherms provide critical insights into the adsorption mechanism, surface properties, and maximum adsorption capacity. The experimental equilibrium data were analyzed using three widely applied isotherm models: Langmuir, Freundlich, and Temkin. These models were fitted to the data, and the parameters were determined from their linearized forms.

3.12.1. Langmuir isotherm model. The Langmuir model assumes monolayer adsorption on a homogeneous surface with equivalent adsorption sites and no lateral interactions between adsorbed molecules. The linearized form is:

$$\frac{C_e}{q_e} = \frac{1}{q_{max} K_L} + \frac{C_e}{q_{max}} \quad (8)$$

where C_e is the equilibrium concentration (mg L^{-1}), q_e is the adsorption capacity at equilibrium (mg g^{-1}), q_{max} is the maximum monolayer adsorption capacity (mg g^{-1}), and K_L is the Langmuir constant (L mg^{-1}) related to the affinity between adsorbent and adsorbate. The dimensionless separation factor R_L is calculated as:

$$R_L = 1/(1 + K_L C_0) \quad (9)$$

where, C_0 is the initial concentration. R_L values between 0 and 1 indicate favorable adsorption. The Langmuir parameters are presented in Table 12.

The Langmuir model demonstrated excellent fit to the experimental data with high correlation coefficients ($R^2 > 0.983$) and low χ^2 values, indicating that monolayer adsorption is the dominant mechanism. The maximum adsorption capacities (q_{max}) followed the order: $Ni(OH)_2$@kaolinite > NiO@kaolinite > Ni@kaolinite, with $Ni(OH)_2$@kaolinite exhibiting the highest capacity (58.6 mg g^{-1} for F^- and 62.1 mg g^{-1} for PO_4^{3-}). The separation factor (R_L) values for all adsorbents ranged between 0.109 and 0.790, confirming favorable adsorption across the entire concentration range studied. The higher K_L values for $Ni(OH)_2$@kaolinite indicate stronger adsorbent–adsorbate affinity, which is attributed to abundant surface hydroxyl groups facilitating ligand exchange and electrostatic interactions.

Table 13 Freundlich isotherm parameters for fluoride and phosphate adsorption

Adsorbent	Ion	K_F ((mg g^{-1}) (L mg^{-1})$^{1/n}$)	n	$1/n$	R^2	χ^2
Ni@kaolinite	F^-	8.52 ± 0.65	2.18	0.459	0.952	2.85
Ni@kaolinite	PO_4^{3-}	9.14 ± 0.72	2.05	0.488	0.948	3.12
NiO@kaolinite	F^-	9.87 ± 0.58	2.31	0.433	0.961	2.34
NiO@kaolinite	PO_4^{3-}	10.5 ± 0.64	2.14	0.467	0.956	2.68
$Ni(OH)_2$@kaolinite	F^-	11.2 ± 0.52	2.45	0.408	0.968	1.92
$Ni(OH)_2$@kaolinite	PO_4^{3-}	12.1 ± 0.58	2.28	0.439	0.963	2.21

3.12.2. Freundlich isotherm model. The Freundlich model describes multilayer adsorption on heterogeneous surfaces with varying adsorption energies. The linearized form is:

$$\log q_e = \log K_F + \frac{1}{n}\log C_e \quad (10)$$

where K_F is the Freundlich constant indicating adsorption capacity ($(mg\ g^{-1})\ (L\ mg^{-1})^{1/n}$), and n is the adsorption intensity factor. Values of $1/n$ between 0 and 1 indicate favorable adsorption, with lower values suggesting greater heterogeneity. The Freundlich parameters are presented in Table 13.

The Freundlich model showed moderate fit with R^2 values ranging from 0.948 to 0.968, which are lower than those obtained for the Langmuir model. The $1/n$ values (0.408–0.488) all fell between 0 and 1, confirming favorable adsorption. The n values greater than 1 (2.05–2.45) indicate that the adsorbents have high adsorption affinity at low equilibrium concentrations. The higher χ^2 values compared to the Langmuir model suggest that the Freundlich model is less suitable for describing the adsorption mechanism, implying that monolayer adsorption on relatively homogeneous surfaces is more representative than multilayer heterogeneous adsorption.

3.12.3. Temkin isotherm model. The Temkin model accounts for adsorbent–adsorbate interactions and assumes that the heat of adsorption decreases linearly with surface coverage. The linearized form is:

$$q_e = B \ln K_T + B \ln C_e \quad (11)$$

where K_T is the Temkin equilibrium binding constant ($L\ mg^{-1}$), $B = RT/b_T$, R is the universal gas constant (8.314 J mol^{-1} K^{-1}), T is temperature (K), and b_T is the Temkin constant related to the heat of adsorption (kJ mol^{-1}). The Temkin parameters are presented in Table 14.

The Temkin model demonstrated good fit with R^2 values ranging from 0.967 to 0.983, indicating that adsorbent–adsorbate interactions play a significant role in the adsorption process. The positive K_T values confirm favorable binding. The b_T values (0.432–0.512 kJ mol^{-1}) are relatively low, suggesting weak to moderate interaction energies consistent with physical adsorption and surface complexation rather than strong chemical bonding. The B values (4.84–5.74) represent the variation in adsorption energy and confirm the heterogeneous nature of the adsorption process to some extent. Overall, Temkin model provided better fit than Freundlich but was still inferior to the Langmuir model; supporting the conclusion that monolayer adsorption on relatively uniform sites is the predominant mechanism.

Table 15 Comparative analysis of isotherm models for $Ni(OH)_2$@kaolinite

Isotherm model	Ion	R^2	χ^2	Model ranking
Langmuir	F^-	0.994	0.45	1st
Langmuir	PO_4^{3-}	0.992	0.58	1st
Temkin	F^-	0.983	1.05	2nd
Temkin	PO_4^{3-}	0.980	1.18	2nd
Freundlich	F^-	0.968	1.92	3rd
Freundlich	PO_4^{3-}	0.963	2.21	3rd

Table 16 Production cost estimation

Component	Cost estimate
Kaolinite raw material	\$50–100 per ton
Nickel precursor	\$20–50 per kg
Synthesis and processing	\$100–200 per kg
Characterization	\$500–1000 (initial)
Total estimated cost	\$200–400 per kg

3.12.4. Isotherm model comparison and mechanistic interpretation. Based on the correlation coefficients and chi-square analysis, the Langmuir model provided the best fit for both fluoride and phosphate adsorption data, followed by Temkin and Freundlich models. The superior fit of the Langmuir isotherm indicates that adsorption occurs predominantly as a monolayer on relatively homogeneous adsorption sites with finite capacity. This conclusion is supported by: (1) high R^2 values (>0.992), (2) low χ^2 values (<0.6), (3) close agreement between experimental and theoretical q_{max} values, and (4) favorable R_L values throughout the concentration range. The moderate fit of the Temkin model suggests that adsorbent–adsorbate interactions contribute to the adsorption process, while the poorer fit of the Freundlich model indicates that multilayer adsorption and extreme surface heterogeneity are not the dominant mechanisms. Integrating the kinetic, thermodynamic, and isotherm findings, the overall adsorption mechanism can be attributed to: (1) monolayer surface complexation on hydroxyl-rich sites (Langmuir behavior), (2) electrostatic attraction between positively charged adsorbent surfaces and anionic fluoride/phosphate species (favorable at pH 6–8), (3) ligand exchange where F^- and PO_4^{3-} replace surface OH^- groups (supported by FT-IR and thermodynamic

Table 14 Temkin isotherm parameters for fluoride and phosphate adsorption

Adsorbent	Ion	K_T ($L\ mg^{-1}$)	b_T (kJ mol^{-1})	B	R^2	χ^2
Ni@kaolinite	F^-	1.42 ± 0.12	0.485	5.11	0.971	1.68
Ni@kaolinite	PO_4^{3-}	1.28 ± 0.11	0.512	4.84	0.967	1.92
NiO@kaolinite	F^-	1.67 ± 0.13	0.458	5.41	0.978	1.32
NiO@kaolinite	PO_4^{3-}	1.51 ± 0.12	0.492	5.04	0.974	1.54
$Ni(OH)_2$@kaolinite	F^-	1.89 ± 0.14	0.432	5.74	0.983	1.05
$Ni(OH)_2$@kaolinite	PO_4^{3-}	1.73 ± 0.13	0.468	5.30	0.980	1.18

Table 17 Operational cost comparison

Adsorbent	Cost per kg	Adsorption capacity (mg g^{-1})	Regeneration cycles	Cost per 1000 L treatment
Ni–kaolinite	$200–400	F^-: 50–100, PO_4^{3-}: 80–120	5–10	$5–10
Activated alumina	$300–500	F^-: 20–40, PO_4^{3-}: 10–30	3–5	$15–25
Iron oxide NPs	$400–600	F^-: 30–60, PO_4^{3-}: 40–70	4–7	$20–30
Biochar	$100–300	F^-: 10–30, PO_4^{3-}: 20–50	2–4	$10–20
Ion-exchange resins	$1000–5000	F^-: 50–80, PO_4^{3-}: 60–100	10–15	$50–100

Table 18 Adsorption efficiency

Parameter	Ni–kaolinite	Activated alumina	Iron oxide	Biochar	Ion-exchange resins
Fluoride uptake	50–100 mg g^{-1}	20–40 mg g^{-1}	30–60 mg g^{-1}	10–30 mg g^{-1}	50–80 mg g^{-1}
Phosphate uptake	80–120 mg g^{-1}	10–30 mg g^{-1}	40–70 mg g^{-1}	20–50 mg g^{-1}	60–100 mg g^{-1}
pH stability	4–9	5–8	3–8	6–9	4–10
Selectivity	High	Moderate	Moderate to high	Low	High

data), and (4) multiple rate-controlling steps including film diffusion, surface adsorption, and intra-particle diffusion (multi-stage kinetic behavior). The thermodynamic parameters (ΔH° < 40 kJ mol^{-1}) confirm that the process involves physical adsorption and surface complexation rather than strong chemisorption (Table 15). Therefore, the combined evidence from kinetic modeling (pseudo second order), thermodynamic analysis (moderate ΔH°), and isotherm fitting (Langmuir best fit) supports a hybrid mechanism dominated by electrostatic interactions and surface complexation.

4. Cost analysis and comparative assessment of advanced nickel-based nanostructured doped kaolinite as a multifunctional adsorbent

The increasing contamination of water bodies with fluoride (F^-) and phosphate (PO_4^{3-}) poses significant environmental and health risks. Conventional remediation techniques such as precipitation, ion exchange, and reverse osmosis are often costly, energy-intensive, or inefficient at low contaminant concentrations. Adsorption-based methods using nanostructured materials have emerged as promising alternatives due to their high efficiency, selectivity, and potential for resource recovery. This study evaluates the cost-effectiveness and comparative performance of nickel-doped nanostructured kaolinite as a multifunctional adsorbent for simultaneous fluoride and phosphate removal. Additionally, we assess its potential for sustainable resource recovery through desorption and regeneration. Ni–kaolinite could achieve <$5 per 1000 L treatment, making it competitive with conventional methods. Tables 16 and 17 show cost analysis.

4.1. Comparative performance assessment

The use of natural kaolinite in Ni–kaolinite reduces reliance on synthetic materials, lowering environmental impacts associated with mining and processing. Nickel doping improves structural stability, preventing metal leaching and ensuring long-term adsorbent safety. Additionally, the ability to recover phosphate from treated water aligns with circular economy principles, transforming waste into a valuable resource for agricultural applications. This approach not only mitigates pollution but also promotes sustainable resource utilization, making Ni–KAO an eco-friendly solution for water remediation. Table 18 shows adsorption efficiency.

5. Conclusions

This study successfully demonstrated the effectiveness of nickel doped kaolinite (Ni@kaolinite and NiO@kaolinite) as multifunctional adsorbents for the efficient remediation of fluoride and phosphate from aqueous systems while enabling sustainable resource recovery. The synthesized catalysts exhibited superior adsorption performance, following pseudo second order kinetics, indicating a adsorption governed by electrostatic attraction and surface complexation interactions supported by moderate enthalpy values. Advanced characterization techniques (XRD, FT-IR, SEM mapping-EDX, BET, and DLS) confirmed the enhanced dispersion of Ni species on the kaolinite support, improving catalytic activity and stability. Ni@kaolinite outperformed NiO@kaolinite, achieving higher removal efficiencies due to improved electron transfer and redox properties. Also, statistical and thermodynamic analyses revealed an endothermic, spontaneous process, optimizing parameters such as pH, temperature, and catalyst dosage. Excellent reusability over ten cycles underscores the material's long-term economic and environmental viability. Phosphate recovery potential aligns with circular economy principles, transforming waste into a reusable resource. These results highlight clay-supported Ni-based catalysts as cost-effective, sustainable, and scalable solutions for industrial wastewater treatment. Future research should focus on large-scale applications, real wastewater testing, and life-cycle assessments to

further validate their industrial feasibility. This work contributes significantly to green chemistry and environmental remediation, offering a promising pathway for pollutant removal and resource recovery.

Author contributions

Aya M. Matloob and Mahmoud F. Mubarak: methodology, formal analysis, data aquation, resources and wrote the original draft. Tahany Mahmoud and Asmaa S. Morshedy: resources, methodology, formal analysis, conceptualization, data curation, investigation, software, validation, visualization, writing – original draft, writing – review, and editing. All authors approved the current and final version of the manuscript for submission.

Conflicts of interest

The authors declare that they have no known competing financial interests or personal relationships that could have appeared to influence the work reported in this paper.

Data availability

All data is available in the manuscript and is available when requested by the corresponding authors.

Acknowledgements

Authors used DeepSeek AI software during the preparation of this work to improve language, readability, and grammar of specific sections. After using this tool, authors reviewed and edited the content as needed and take full responsibility for the content of published manuscript.

References

1 T. E. Oladimeji, *et al.*, Review on the impact of heavy metals from industrial wastewater effluent and removal technologies, *Heliyon*, 2024, **10**(23), e40370.
2 H. R. Ahmed, Heterogeneous catalysts in advanced oxidation processes: A comprehensive review on antibiotic removal from wastewater, *Sep. Purif. Technol.*, 2025, **374**, 133670.
3 V. Kumar, *et al.*, Removal of Inorganic Pollutants from Wastewater: Innovative Technologies and Toxicity Assessment, *Sustainability*, 2023, **15**, 16376.
4 H. W. Ahmad, *et al.*, Sustainable Wastewater Treatment Strategies in Effective Abatement of Emerging Pollutants, *Water*, 2024, **16**, 2893.
5 E. Sanad, *et al.*, Tailored alginate nanocomposite beads for efficient heavy metals sequestration from industrial wastewater, *Int. J. Environ. Anal. Chem.*, 2026, **106**(5), 1115–1141.
6 A. S. Morshedy, A. M. A. El-Naggar and M. T. Zaky, Sonophotocatalytic reformation: Transforming paraffin wax into hydrogen-rich fuel, *Int. J. Hydrogen Energy*, 2026, **223**, 154271.
7 M. A. A. El-Khair, *et al.*, Harvesting the synergistic effect of $CuFe_2O_4$@Ni-MOF nanomagnetic photocatalyst for enhanced visible light-driven green hydrogen production, *Int. J. Hydrogen Energy*, 2025, **101**, 280–294.
8 A. S. Morshedy, *et al.*, Ni@$CaTiO_3$ Nanocomposites for Methane Decomposition Into Hydrogen and Multiwalled Carbon Nanotubes, *ChemistrySelect*, 2024, **9**(32), e202401908.
9 F. Huang, *et al.*, Catalytic performances of Ni/mesoporous SiO_2 catalysts for dry reforming of methane to hydrogen, *J. Energy Chem.*, 2016, **25**(4), 709–719.
10 Y. Cai, *et al.*, Recent Advances in Ni-Based Catalysts for CH_4-CO_2 Reforming (2013–2023), *Atmosphere*, 2023, **14**, 1323.
11 K. S. Mohammed, *et al.*, Synthesis of Kaolin-Supported Nickel Oxide Composites for the Catalytic Oxidative Degradation of Methylene Blue Dye, *ACS Omega*, 2024, **9**(4), 4287–4299.
12 M. A. Abo El-Khair, A. S. Morshedy and A. G. Al-Gamal, Synergistic enhancement of photocatalytic hydrogen evolution via NiS_X-NiO/S-g-C_3N_4 heterojunctions under visible light irradiation, *Fuel*, 2026, **413**, 138239.
13 H. M. Abd El Salam and A. S. Morshedy, TiO_2@Metal organic framework $Ni_2(BDC)_2(DABCO)$ as an efficient water splitting heterogeneous photocatalyst for enhanced green hydrogen generation under visible light, *Int. J. Hydrogen Energy*, 2025, **151**, 150142.
14 O. B. Ayodele, Effect of phosphoric acid treatment on kaolinite supported ferrioxalate catalyst for the degradation of amoxicillin in batch photo-Fenton process, *Appl. Clay Sci.*, 2013, **72**, 74–83.
15 J. D. D. Melo, *et al.*, Effects of thermal and chemical treatments on physical properties of kaolinite, *Ceram. Int.*, 2010, **36**(1), 33–38.
16 A. K. Panda, *et al.*, Effect of sulphuric acid treatment on the physico-chemical characteristics of kaolin clay, *Colloids Surf., A*, 2010, **363**(1), 98–104.
17 T. A. Sokolova, *et al.*, The Effect of Treatment with Hydrogen Peroxide and the Mehra–Jackson Reagent on X-ray Diffraction Patterns of Clay Fractions, *Eurasian Soil Sci.*, 2017, **50**(12), 1386–1394.
18 K. S. Mohammed and M. Atlabachew, Synthesis of Kaolin-Supported Nickel Oxide Composites for the Catalytic Oxidative Degradation of Methylene Blue Dye, *ACS Omega*, 2024, **9**(4), 4287–4299.
19 H. A. El-Sabban, M. F. Mubarak and M. A. Diab, PPy-NTs/C/TiO_2/poly(ether sulfone) porous composite membrane: Efficient ultrafiltration of Evans blue dye from industrial wastewater, *Synth. Met.*, 2023, **297**, 117383.
20 A. El-Denglawey, M. F. Mubarak and H. Selim, Tertiary Nanocomposites of Metakaolinite/Fe_3O_4/SBA-15 Nanocomposite for the Heavy Metal Adsorption: Isotherm and Kinetic Study, *Arabian J. Sci. Eng.*, 2022, **47**(1), 455–476.
21 W. Plazinski, J. Dziuba and W. Rudzinski, Modeling of sorption kinetics: the pseudo-second order equation and the sorbate intraparticle diffusivity, *Adsorption*, 2013, **19**(5), 1055–1064.

22 E. D. Revellame, *et al.*, Adsorption kinetic modeling using pseudo-first order and pseudo-second order rate laws: A review, *Cleaner Eng. Technol.*, 2020, **1**, 100032.
23 S. S. M. Rodrigues, *et al.*, Immobilization of Distinctly Capped CdTe Quantum Dots onto Porous Aminated Solid Supports, *ChemPhysChem*, 2015, **16**(9), 1880–1888.
24 M. Vigdorowitsch, *et al.*, Freundlich Isotherm: An Adsorption Model Complete Framework, *Appl. Sci.*, 2021, **11**, 8078.
25 S. Akash, *et al.*, Metal oxide nanobiochar materials to remediate heavy metal and dye pollution: a review, *Environ. Chem. Lett.*, 2024, **22**(4), 2091–2112.
26 W. Rahmalia, *et al.*, Stability, reusability, and equivalent circuit of TiO_2/treated metakaolinite-based dye-sensitized solar cell: effect of illumination intensity on V_{oc} and I_{sc} values, *Mater. Renew. Sustain. Energy*, 2021, **10**(2), 10.
27 I. Shakir, *et al.*, Nickel hydroxide nanoparticles and their hybrids with carbon nanotubes for electrochemical energy storage applications, *Results Phys.*, 2020, **17**, 103117.
28 S. Dekkar, *et al.*, Dry Reforming of Methane over Ni–Al_2O_3 and Ni–SiO_2 Catalysts: Role of Preparation Methods, *Catal. Lett.*, 2020, **150**(8), 2180–2199.
29 T. A. Aragaw and F. T. Angerasa, Synthesis and characterization of Ethiopian kaolin for the removal of basic yellow (BY 28) dye from aqueous solution as a potential adsorbent, *Heliyon*, 2020, **6**(9), e04975.
30 V. Biju and M. Abdul Khadar, Fourier transform infrared spectroscopy study of nanostructured nickel oxide, *Spectrochim. Acta, Part A*, 2003, **59**(1), 121–134.
31 C. Kavitha, *et al.*, RETRACTED: Elimination of Lead by Biosorption on Parthenium stem powder using Box-Behnken Design, *S. Afr. J. Chem. Eng.*, 2022, **42**, 270–279.
32 H. Tahir, S. Atika and S. Muhammad, Synthesis of Kaolin Loaded Ag and Ni Nanocomposites and Their Applicability for the Removal of Malachite Green Oxalate Dye, *Iran. J. Chem. Chem. Eng.*, 2018, **37**(3), 11–22.
33 A. Moumen, *et al.*, Removal of Malachite Green Dye from Aqueous Solution by Catalytic Wet Oxidation Technique Using Ni/Kaolin as Catalyst, *Molecules*, 2022, **27**, 7528.
34 W. Li, *et al.*, Sulfate assisted synthesis of α-type nickel hydroxide nanowires with 3D reticulation for energy storage in hybrid supercapacitors, *Mater. Chem. Front.*, 2022, **6**(1), 94–102.
35 D. S. Hall, *et al.*, Applications of in situ Raman spectroscopy for identifying nickel hydroxide materials and surface layers during chemical aging, *ACS Appl. Mater. Interfaces*, 2014, **6**(5), 3141–3149.
36 N. Mironova-Ulmane, *et al.*, Polarisation dependent Raman study of single-crystal nickel oxide, *Open Phys.*, 2011, **9**(4), 1096–1099.
37 D. Egirani, *et al.*, Synthesis and characterization of kaolinite coated with copper oxide and its effect on the removal of aqueous Lead(II) ions, *Appl. Water Sci.*, 2019, **9**(4), 109.
38 V. O. Shikuku and T. Mishra, Adsorption isotherm modeling for methylene blue removal onto magnetic kaolinite clay: a comparison of two-parameter isotherms, *Appl. Water Sci.*, 2021, **11**(6), 103.
39 A. A. Adeyemo, I. O. Adeoye and O. S. Bello, Adsorption of dyes using different types of clay: a review, *Appl. Water Sci.*, 2017, **7**(2), 543–568.
40 L. Mao, *et al.*, Ultrathin $Ni(OH)_2$ nanosheets: a new strategy for cocatalyst design on CdS surfaces for photocatalytic hydrogen generation, *RSC Adv.*, 2019, **9**(3), 1260–1269.
41 K. Aimdate, *et al.*, Natural Kaolin-Based Ni Catalysts for CO_2 Methanation: On the Effect of Ce Enhancement and Microwave-Assisted Hydrothermal Synthesis, *ACS Omega*, 2021, **6**(21), 13779–13794.
42 A. Muthuvel, *et al.*, Biosynthesis of gold nanoparticles using Solanum nigrum leaf extract and screening their free radical scavenging and antibacterial properties, *Biomed. Prev. Nutr.*, 2014, **4**(2), 325–332.
43 R. Greenwood, *et al.*, The zeta potential of kaolin suspensions measured by electrophoresis and electroacoustics, *Chem. Pap.*, 2007, **61**(2), 83–92.
44 M. H. Cambre, *et al.*, Cytotoxicity of NiO and $Ni(OH)_2$ Nanoparticles Is Mediated by Oxidative Stress-Induced Cell Death and Suppression of Cell Proliferation, *Int. J. Mol. Sci.*, 2020, **21**(7), 2355.
45 K. J. Chaudhary, *et al.*, Enhanced hydrogen production through methane dry reforming: Evaluating the effects of promoter-induced variations in reducibility, basicity, and crystallinity on Ni/ZSM-5 catalyst performance, *Energy Convers. Manage.: X*, 2024, **23**, 100631.
46 G. Salehi and M. Bagherzadeh, Visible Light-Driven Photocatalytic Degradation of Methylene Blue Dye Using a Highly Efficient Mg-Al LDH@g-C_3N_4@Ag_3PO_4, *Nanocomposite*, 2024, **9**(4), 4581–4593.
47 E. Torrik, M. Soleimani and M. T. Ravanchi, Application of Kinetic Models for Heavy Metal Adsorption in the Single and Multicomponent Adsorption System, *Int. J. Environ. Res.*, 2019, **13**(5), 813–828.
48 J. López-Luna, *et al.*, Linear and nonlinear kinetic and isotherm adsorption models for arsenic removal by manganese ferrite nanoparticles, *SN Appl. Sci.*, 2019, **1**(8), 950.
49 M. F. Mubarak, *et al.*, Meta-kaolinite metal oxide quaternary composite for layered double hydroxide applied to a new frontier in adsorption technology: Synthesis, adsorption performance and kinetics study, *Inorg. Chem. Commun.*, 2025, **178**, 114647.